Hydrodynamic instabilities of a dual-mode air/SF_6 interface induced by a cylindrically convergent shock

Yu Liang[1,2], Lili Liu[1,2], Xisheng Luo[1†], Chih-yung Wen[3‡]

[1]Advanced Propulsion Laboratory, Department of Modern Mechanics, University of Science and Technology of China, Hefei 230026, China

[2]NYUAD Research Institute, New York University Abu Dhabi, Abu Dhabi 129188, UAE

[3]Department of Aeronautical and Aviation Engineering, The Hong Kong Polytechnic University, Kowloon, Hong Kong

Experiments on a two-dimensional dual-mode air/SF_6 interface with controllable initial conditions are performed in a cylindrically convergent shock tube to examine the dependence of perturbation growth on the initial spectrum. The hydrodynamic instabilities, including the Richtmyer-Meshkov (RM) instability and the additional Rayleigh-Taylor (RT) effect, imposed by the convergent shock wave on the dual-mode interface are focused. The mode-coupling between the two initially constituent modes before the reshock is highlighted. It is evident that the amplitude growths of all first-order modes and second-order harmonics and couplings depend on the variance of the interface radius and are influenced by the mode-coupling from the very beginning. It is confirmed that the mode-coupling mechanism is closely related to the initial spectrum, including azimuthal wavenumbers, relative phases and initial amplitudes of the constituent modes. By considering the geometry convergence, the mode-coupling effect, and other physical mechanisms, a series of second-order nonlinear solutions are adopted to predict the RM instability and the additional RT effect in the cylindrical geometry, reasonably quantifying the amplitude growth of each mode, harmonic and coupling. Numerical simulations further validate the nonlinear solutions considering various initial spectrums. Last, the conditions for suppressing the hydrodynamic instabilities of different frequency modes are summarised.

Introduction

Richtmyer-Meshkov (RM) instability occurs when an interface separating two fluids with different densities is accelerated by a shock wave, then bubbles (lighter fluids penetrating heavier ones) and spikes (heavier fluids penetrating lighter ones) arise, and the turbulence might be finally induced . RM instability was first theoretically investigated by and then experimentally confirmed by in the planar geometry. RM instability is generally regarded as the special Rayleigh-Taylor (RT) instability at an impulsive limitation. As reviewed by , RM instability plays an essential role in various industrial and scientific fields, including inertial confinement fusion (ICF), supernova explosions, ejecta, material strength, chemical reactions, solar prominence, and ionospheric flows. The RM instability on a single-mode interface has been extensively studied due to its fundamental significance . Nevertheless, the initial perturbations on the surfaces in applications are essentially multi-mode with wavenumbers spanning many orders of magnitude . The relationship between the multi-mode RM instability and the initial spectrum remains unclear. Furthermore, the ICF and other applications care more about the hydrodynamic instabilities in the cylindrical and spherical geometries . Due to its significance, research on the multi-mode RM instability induced by a convergent shock is urgently needed.

Past studies on the planar multi-mode RM instability have shown that when the local perturbation on a multi-mode interface originated from the superposition of multiple modes becomes comparable to its wavelength, the mode-coupling between the multiple modes has an important influence on the instability development . The following theoretical, experimental, and numerical works on the planar multi-mode RM instability are introduced below.

I) Theoretically, first proposed a modal model with second-order accuracy to quantify the influence of the mode-coupling between the multiple modes on the RT instability. The modal model and its extended types have achieved a wide range of validation in the issues of RT instability and RM instability . Assuming that the mode-coupling is absent before each bubble of a multi-mode RM unstable interface reaches its asymptotic growth, proposed a statistical potential flow model to predict the eventual average bubble distribution and bubble amplitude growth rate. However, the potential flow model is invalid when the two fluids' densities are similar. Subsequently, proposed the vortex model to make up the bubble asymptotic growth rate when the density ratio of the two fluids approaches 1. Both the potential flow model and the vortex model acquire a self-similar growth of the bubble amplitude independent of the initial spectrum. Later, the perturbation expansion model was extended by to predict the early nonlinear amplitude growths of the constituted modes of a multi-mode RM unstable interface by retaining the terms with the highest power in time. Recently, the Group theory approach has been proven to identify the connection between the symmetry properties of the interface morphology and the relative phases of the modes constituting the interface spectrum.

II) Experimentally, performed the first shock tube experiments to investigate the two-bubble competition and found that the bubbles with a larger size expand and rise faster, whereas the bubbles with a smaller size shrink and are swept downstream into the spikes of surviving bubbles. conducted a series of three-dimensional (3-D) linear electric motor experiments to investigate the multi-mode RT and RM instabilities. They found that the density ratio has a limited effect on the self-similar growth factor θ for the bubble. When the density ratio is large, the θ for the spike is larger than the bubble counterpart. investigated the multi-mode RM instability of two liquids and found that the development of the multi-mode perturbation strongly depends on the amplitudes of the initially constituent modes. argued that the growth of the multi-mode perturbation created by a gas curtain shows a weak dependence on the initial spectrums. performed the RM instability experiments of a dual-mode interface under high-Mach-number conditions. The results indicated that new harmonics are generated from the mode-coupling between the two initially constituent modes, and the perturbations of these modes grow and saturate over time. The dual-mode RM instability under weak shock conditions was considered by , from which the mode-coupling effect on the RM instability cannot be ignored when the wavenumber of one constituted mode is twice the wavenumber of the other constituted mode. experimentally investigated the mixing of a multi-mode RM unstable interface using density and velocity statistics and found that the flow shows distinct memory of initial conditions. The long-wavelength perturbation has a strong influence on the interface development. examined the RM instability on four quasi-single-mode interfaces created by the soap film technique in the early nonlinear stage. The effect of initially constituent high-order modes on the multi-mode RM instability was highlighted to distinguish the multi-mode RM instability from the single-mode counterpart. further confirmed that the RM instability of a quasi-single-mode interface still has memory on the initial spectrum even though the interface is shocked twice. generated a near-sinusoidal interface dominated by one mode with a novel membraneless technique where cross-flowing air is separated from SF_6 by an oscillating splitter plate. Earlier mixing transitions for higher amplitude-wavelength ratio cases were noted from the experiments. investigated the RM instability on a multi-mode air/SF_6 interface initially dominated by three modes. It was revealed that the mode-coupling is closely related to the initial spectrum and plays an essential role in RM flows from the very beginning if the initial amplitudes of the constituent modes are large. examined the differences between the effects of bubble competition and spike competition on the multi-mode RM instability and concluded that the bubble competition suppresses instability of the small-wavelength perturbation more than the spike competition.

III) Numerically, it is commonly realised that the phases of the constituted modes influence the multi-mode perturbation growth . Besides, the self-similar growth factor θ of the late-time RM instability depends on the scale of the initial spectrum. Although the values of θ in many high-fidelity simulations, including the extensive collaborations of the θ-group , have not been unified, it is widely accepted that the broadband perturbation leads to a larger bubble growth factor than the narrowband counterpart .

The convergent RM instability, involving initial conditions relevant to the ICF, has become increasingly attractive in recent years . Compared with the planar RM instability, the convergent RM instability involves more physical mechanisms. First, the unique geometric convergence inevitably influences the convergent RM instability. For example, in a high-gain ICF target, the ratio of the initial outer target radius to the final hot-spot radius is up to $\sim 30-40$. Second, the additional RT effect induced by the acceleration or deceleration of the interface complicates the interface evolution and results in the interface being more unstable or stable. Third, the compressibility of the post-shock flow further influences the instability. The other theoretical, experimental, and numerical works on the convergent RM instability are introduced below.

I) Theoretically, based on the small perturbation assumption, and separately derived the linear solutions for the convergent RM instability in the cylindrical and spherical geometries. It was found that the interface amplitude growth rate varies with the radius of the shocked interface, which is later called the Bell-Plesset effect. further considered the case where the densities of the two fluids change uniformly with time. Later, deduced a compressible linear solution for the convergent RM instability accounting for the fluid compression. examined the convergent RM instability of multiple interfaces in cylindrical and spherical geometries and proposed a numerical method to solve the eigenvalue problems of the convergent RM instability on the arbitrary number of stratified fluids. In the same order of the geometry convergence, separately listed the linear solutions for the planar, cylindrically convergent, and spherically convergent RM instability using the impulsive acceleration assumption as,

$$a_n = a_n^0[1 + \mathrm{kA\Delta vt}],$$

$$a_n = a_n^0\left[1 + (nA - 1)(1 - \frac{R_i^0}{R_i})\right],$$

$$a_n = a_n^0\left\{1 + \left[\frac{n(n+1)A}{2n + 1 - A} - 1\right]\left[1 - (\frac{R_i^0}{R_i})^2\right]\right\},$$

where a_n and a_n^0 are the time-varying amplitude and the initial amplitude of the single-mode perturbation with the azimuthal wavenumber n ($\equiv kR_i$), respectively; k is the wavenumber of the single-mode perturbation; R_i and R_i^0 are the time-varying radius and the initial radius of the interface, respectively; Δv is the velocity jump of the interface induced by the shock; and A (defined as $(\rho^{\mathrm{ex}} - \rho^{\mathrm{in}})/(\rho^{\mathrm{ex}} + \rho^{\mathrm{in}})$, with ρ^{ex} and ρ^{in} being the density of the external fluid located at a radius r of $r > R_i$ and the density of the inner fluid located at $R_i > r > 0$, respectively, as sketched in figure 1(d)) is the Atwood number. Assuming that the interface moves uniformly, i.e., $R_i = R_i^0 + \Delta vt$, equations ([cylindricalRMI]) and ([sphericalRMI]) separately for the cylindrically and spherically convergent RM instability reduce to equation ([planarRMI]) for the planar RM instability at a large R_i. Recently, based on the perturbation expansion method, derived a fourth-order weakly nonlinear solution for the RM instability of a single-mode interface at a fixed radial position in the cylindrical geometry, highlighting the cylindrical geometry effect on bubbles and spikes under different A conditions. Subsequently, extended the validity range of the weakly nonlinear solution to the late nonlinear stage based on Padé approximation, and which agrees well with the numerical results of . proposed a weakly nonlinear solution for the cylindrically convergent RM instability of a uniformly imploding or exploding single-mode interface. The perturbation growths of the first three order harmonics and the high-order feedback to the fundamental mode were quantified.

II) Experimentally, used double exposure holographic interference technology to capture the interaction of a cylindrically convergent shock and a gas cylinder with various species in an annular vertical diaphragmless shock tube. The perturbation width growth rate of the reshocked interface in the cylindrical geometry was found to be larger than that in the planar geometry. Recently, and improved the interface formation and flow visualisation methods in the same kind shock tube. The interactions of a cylindrically convergent shock and various polygonal and sinusoidal air/SF_6 interfaces were experimentally investigated. Based on the gas lens method to convert a planar shock to a convergent shock, the cylindrically convergent RM instability on the single-mode SF_6/air interface and air/SF_6 interface were separately investigated. The influence of the supports utilised to form the initial nitrocellulose interface on the RM flow was concerned . Recently, extended the gas lens method to generate a spherically convergent shock and showed the potential to perform spherically convergent RM instability experiments. designed a curved solid wall with a specific shape to directly convert a planar shock to a cylindrically convergent shock according to the shock dynamics in a horizontal shock tube. Subsequently, the interactions of a cylindrically convergent shock and various interfaces, including gas bubbles, gas cylinders, inclined interfaces and sinusoidal interfaces, were experimentally investigated in this shock tube . In these works, studied the convergent RM instability on a 3-D air/SF_6 single-mode interface with a minimum-surface feature. They observed the interface deceleration due to the high pressure near the geometric centre. It was proved that the interface deceleration leads to the additional RT effect superposed on the evolving interface, resulting in a rapid decrease in the interface amplitude, and even causing the phase reversal of the interface before the reshock. To eliminate the interface deceleration and the additional RT effect, transferred the cylindrically convergent shock to a planar one when the transmitted shock is near the geometric centre, avoiding the high pressure near the geometric centre. Recently, the shock dynamics method has been extended to generate a spherically convergent shock and a cylindrically divergent shock . Moreover, designed a semi-annular horizontal shock tube to generate a cylindrically convergent shock and showed its great potential in studying the convergent RM instability due to the convenience of forming shape-controllable gaseous interfaces. Subsequently, examined the time-varying interface displacement of a shocked unperturbed air/SF_6 interface and the amplitude growths of a single-mode air/SF_6 interface with various amplitude-wavelength-ratios in this shock tube. Recently, a series of experimental studies on the hydrodynamic instabilities of a gas layer driven by a cylindrically convergent shock has been conducted in this shock tube . It was revealed that the mode-coupling between the two interfaces of the gas layer and the reverberating waves inside the gas layer have non-negligible influences on the gas layer evolution.

III) Numerically, discovered the scaling laws for the RM unstable interface driven by a strong cylindrically convergent shock. Later, performed a series of simulations on the RM instability of a single-mode interface driven a cylindrically convergent or divergent shock and observed the complex instability development after the reshock. numerically investigated the interface evolution using the vortex dynamics method in the cylindrical geometry. They analysed the curvatures of bubbles and spikes as well as the vorticity strength and circulation on the evolving interface. studied the linear evolution of the convergent RM instability and deduced a unified expression for the asymptotic growth rate of the planar, cylindrical and spherical RM instability, highlighting the influence of the geometric convergence on the perturbation growth rate. performed the large-eddy simulation on the spherically convergent RM instability. It was found that the reshock mixing on an air/SF_6 interface is enhanced by the reverberating shocks between the interface and the geometric centre, which is different from the planar RM instability that is enhanced by the reverberating rarefaction waves between the interface and the reflection wall. compared their simulations with the experiments of using the direct numerical simulation method. They concluded that both qualitative and quantitative consistencies between simulations and experiments could be achieved before the reshock provided that the premixed width of the interface is taken into account. investigated the convergent RM instability in cylindrical and spherical geometries using the implicit large eddy simulation method, highlighting the differences in the statistical characteristics of turbulent mixing between the cylindrically and spherically convergent RM instability. investigated the cylindrically convergent RM instability with and without chemical reactions using the direct numerical simulation method to explore the influence of chemical reactions on the statistical characteristics of transition and turbulent mixing.

From the reviews of the multi-mode RM instability and the convergent RM instability, it is evident that the RM instability is related to the initial spectrum and the geometric domain. However, the quantitative relation between initial conditions and the multi-mode RM instability driven by a convergent shock is still unclear. On the one hand, elaborate convergent shock tube experiments on the multi-mode RM instability with controllable initial conditions are very limited. On the other hand, analytical models for predicting the multi-mode RM instability in cylindrical and spherical geometries are rare. In this work, a two-dimensional (2-D) multi-mode interface constituted of two dominant modes is first formed with the extended soap film technique. An elaborate experiment on an air/SF_6 dual-mode interface is then conducted in the semi-annular horizontal shock tube. Numerical simulations are performed to provide quantitative data considering more initial conditions. Later, a series of analytical, nonlinear solutions with second-order accuracy are adopted to quantify the hydrodynamic instabilities, including the RM instability and the additional RT effect, imposed on the dual-mode interface before the reshock. Last, the connections between the hydrodynamic instabilities and initial spectrums are explored.

Experimental and numerical methods

Experimental setup

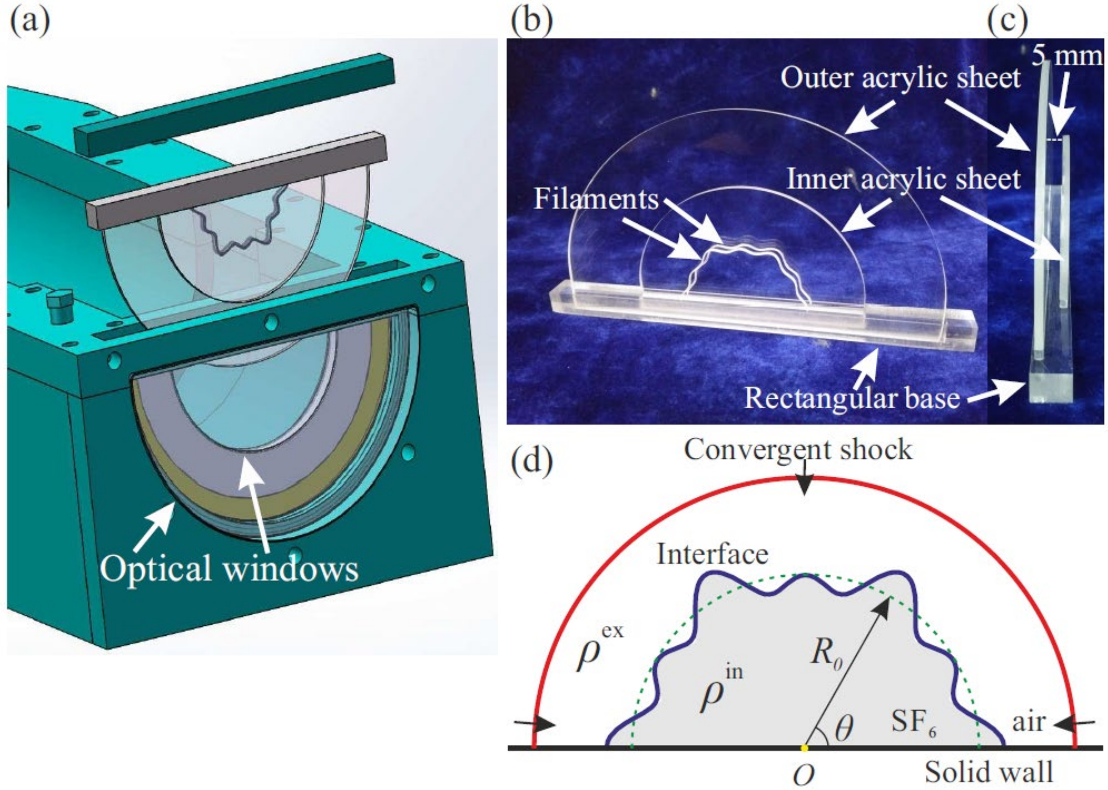

Figure 1 (a) The sketch of the test section of the semi-annular shock tube, (b) the front view and (c) the side view of the interface formation device, and (d) the experimental configuration for a cylindrically convergent shock impacting a dual-mode air/SF_6 interface, where R_i^0 denotes the radius of the balanced position of the initial dual-mode interface; O denotes the geometric centre; ρ^{ex} and ρ^{in} denote the densities of the fluids located at a radius r of $r > R_i$ and $R_i > r > 0$, respectively.

The experiment is carried out in a semi-annular convergent shock tube originally designed by , which has exhibited good feasibility and reliability in producing a cylindrically convergent shock . Benefiting from the open test section, as sketched in figure 1(a), a removable interface formation device can be efficiently designed in which a shape-controllable gaseous interface can be generated using the extended soap film technique. The soap film technique can essentially eliminate the additional short-wavelength perturbations, diffusion layer and three-dimensionality . As shown in figures 1(b) and (c), a device consisting of two semi-circular transparent acrylic sheets with a spacing of 5.0 mm is fixed on a rectangular base. Two micro-channels (with a width of 0.50 mm and a depth of 0.20 mm) with a designed dual-mode shape are precisely graved on the opposite surfaces of the two acrylic sheets. Two acrylic filaments (with a width of 0.45 mm and a height of 0.40 mm) with the same dual-mode shape are embedded separately in the micro-channels to introduce two small bulges on the plate surfaces to restrict the soap film. Subsequently, a soap bubble full of SF_6 is blown within two plates until the soap film comes in contact with the bulges. After this, the whole device is immediately inserted into the test section and equipped tightly with optical windows, as shown in figure 1(a).

The experimental configuration is sketched in figure 1(d), where a cylindrically convergent shock moves inward and later impacts the dual-mode interface. In a polar coordinate system, the initial interface can be parameterised as

$$r = R_i^0 + a_{n_1}^0 \cos(n_1\theta) + a_{n_2}^0 \cos(n_2\theta),$$

where R_i^0 equals 26.0 mm; n_1 and n_2 denote the azimuthal mode numbers of the two initially constituent modes and equal 6 and 12, respectively, in the experiment; and the initial amplitudes of mode n_1 ($a_{n_1}^0$) and mode n_2 ($a_{n_2}^0$) equal 1.0 mm.

The ambient pressure and temperature are 101.33 kPa and 293.15 K, respectively. The ambient gas is air, and the test gas is a mixture of air and SF_6. The mass fraction of SF_6 is deduced as 91.1%. The Atwood number A is -0.57 in this study. The flow field is illuminated by a DC-regulated light source (CEL-HXF300, the maximum power output is 249 W) and captured by schlieren photography combined with a high-speed camera (FASTCAM SA5, Photron Limited, full resolution of 1024×1024). The camera's frame rate is 87,500, corresponding to a time interval of 11.43 $\umu$s. The exposure time is 1 $\umu$s. The pixel resolution is 0.26 mm·pixel^{-1}. In the experiment, the shock velocity at the time of the impact with the interface cannot be obtained precisely due to the limitation of temporal resolution. However, the Mach number of the incident shock at a radius of 34.0 mm, i.e., before the shock reaches the interface, can be measured to be 1.29 ± 0.01. The increment of the shock Mach number between that instant and when the shock reaches the interface is about 0.03, according to the Chester-Chiness-Whitham relations . As a result, the Mach number of the incident converging shock at the interface's impact time is evaluated to be 1.32 ± 0.01. Based on the one-dimensional (1-D) gas dynamics theory , when the shock impacts the initial interface, the velocity of the incident shock (v_s) is -457 m·s^{-1}, the velocity of the transmitted shock (v_t) is -236 m·s^{-1}, the velocity of the reflected shock (v_f) is 407 m·s^{-1}, and the velocity jump of the interface (Δv) is -123 m·s^{-1}.

Numerical scheme

Numerical simulations are performed to obtain the detailed flow field required for an in-depth analysis of flow regimes. The process of a cylindrically convergent shock interacting with a gaseous interface examined in this study is described by compressible Euler equations, which coincide with the numerical studies focusing on the early to intermediate regimes of RM instability with or without the reshock . An upwind space-time conservation elements/solution elements (CE/SE) scheme is utilised with second-order accuracy in both space and time . A volume-fraction-based five-equation model is used to illustrate the different species residing on both sides of the inhomogeneous interface. The contact discontinuity restoring Harten-

Lax-van Leer-Contact Riemann solver is used to determine the numerical fluxes between the conservation elements. The use of this scheme in capturing shocks and details of complex flow structures for the RM instability issues and shock-droplet interactions has been well validated . A comprehensive review of the numerical scheme and its extensive applications was recently reported by .

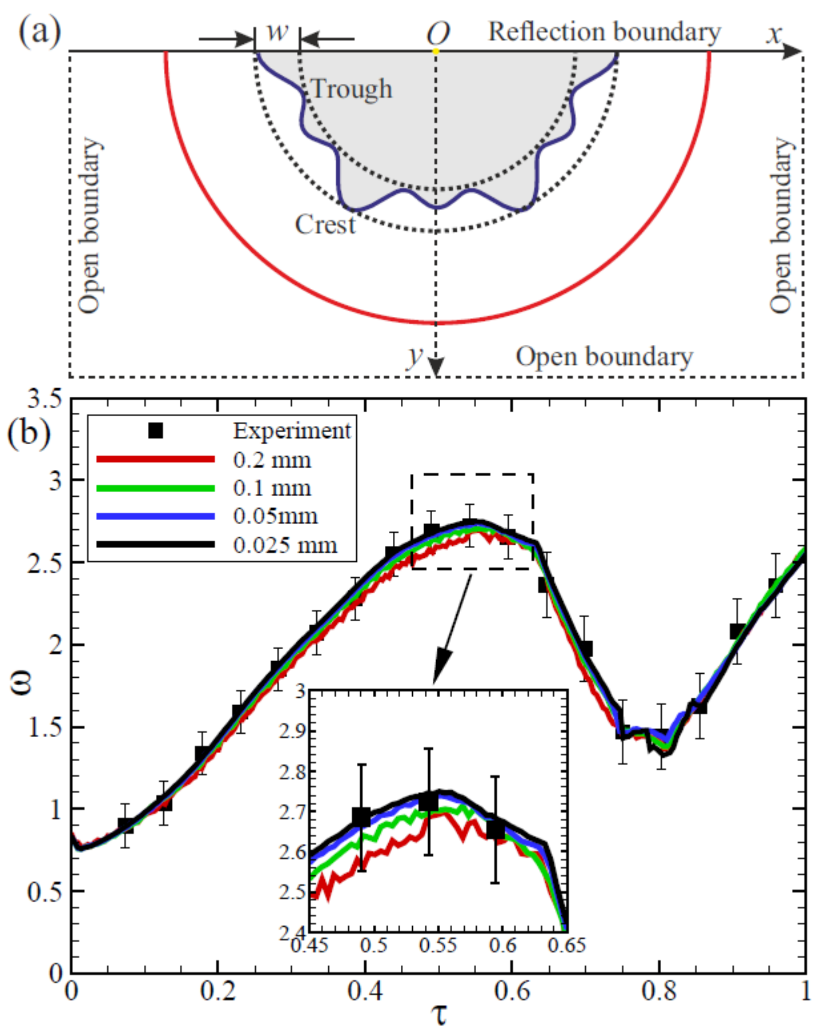

Figure 2. (a) The schematic of the numerical setup, with w denoting the perturbation width of the dual-mode interface, and (b) comparisons of the dimensionless perturbation width of the dual-mode interface between the experimental results and numerical results at different mesh sizes. The red semi-circle in (a) at r = 34 mm indicates the initial imploding shock of Mach number 1.29.

The initial settings of the 2-D simulation are presented in figure 3(a). Open boundary conditions, which apply a zeroth-order extrapolation of physical quantities to ghost points, are enforced on the left, right, and bottom boundaries ($x = -100.0$, $x = 100.0$ and $y = 50.0$ mm), respectively, to eliminate the waves reflected from the left, right and bottom boundaries . Reflection conditions are imposed at the top boundary ($y = 0$). The density and specific heat ratio of the ambient gas outside the perturbed gas cylinder are 1.20 $kg \cdot m^{-3}$ and 1.40, respectively; and the density and specific heat ratio of the test gas inside the perturbed gas cylinder are 4.46 $kg \cdot m^{-3}$ and 1.24, respectively. The initially incident shock wave is set to travel inward with a Mach number of 1.29 and a radius of 34.0 mm, as sketched in figure 3(a). The initial post-shock flow is supposed to be uniform and calculated according to the Rankine-Hugoniot relation, which coincides with the recent numerical studies on the convergent RM instability .

Code validation

For the data obtained from numerical simulations, since the mass fraction of SF_6 in the test gas is decided by the experiment as 91.1%, we choose the nodes with a mass fraction of SF_6 between 1.0% and 90.0% as the interfacial contour. Then, the mean radius of these nodes on each azimuthal angle is taken as the average position of the local interface. The perturbation width of a dual-mode interface, w, is defined as the radial distance between the crest and trough of the dual-mode interface, as sketched in figure 3(a).

The time-varying dimensionless perturbation width of the dual-mode interface is measured from our experiment, as shown with solid symbols in figure 3(b). The moment when the incident shock reaches the radius of R_i^0 is defined as $t = 0$. Time is scaled as $\tau = tv_t/R_i^0$, and perturbation width is scaled as $\omega = w/w_0$, where w_0 denotes the initial perturbation width of the dual-mode interface and equals 3.12 mm in the experiment. It can be found that the current numerical results, as shown with lines in figure 3(b), quantitatively agree well with the experimental results. Four mesh sizes of 0.20 mm, 0.10 mm, 0.05 mm and 0.025 mm are tested for the grid-convergence validation. The time-varying dimensionless perturbation widths of the dual-mode interface converge when the mesh size is reduced to 0.05 mm and 0.025 mm in the numerical simulations. Therefore, an initial mesh size of 0.05 mm is adopted for all simulations to ensure accuracy and minimise the computational cost.

Qualitative analysis

The initial dual-mode interface (II) in the experiment has a short-wavelength spike (SS) in the middle with two long-wavelength spikes (LS) located on its two sides, as shown in figure 4. Before the shock impacts the interface (-7 $\umu$s), the initial interface in the schlieren image seems thick because the interface is covered by two dual-mode micro-channels (0.5 mm in width) engraved on the transparent acrylic sheets. First, when the incident shock (IS) passes across the interface, the shock bifurcates into an inward-moving transmitted shock (TS) and an outward-moving reflected shock (IRS). Subsequently, the shocked interface (SI) leaves its original location, and a density-gradient interface with a perfect dual-mode shape can be observed (16 $\umu$s). As time proceeds, the interface undergoes sustained deformation due to the deposition of baroclinic vorticity induced by the incident shock and the geometry convergence . Although the perturbation on the TS decreases as the TS converges, the ratio of the perturbation to the radius of the TS increases . As a result, the front of the convergent TS becomes polygonal , and the transverse waves (TW) behind the transmitted shock are prominent (see 85 $\umu$s).

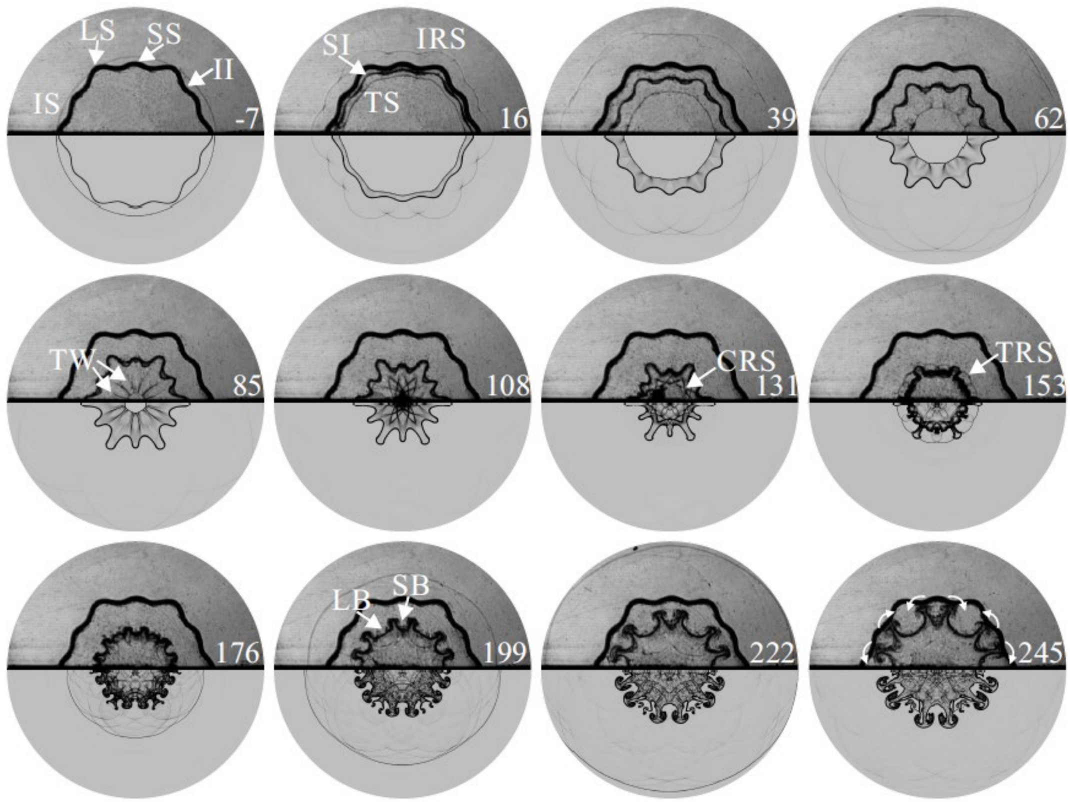

Figure 3 Typical schlieren images obtained from the experiment (top half of each image) and simulation (bottom half), where IS denotes the incident convergent shock, II denotes the initial interface, LS denotes the long-wavelength spike, SS denotes the short-wavelength spike, LB denotes the long-wavelength bubble, SB denotes the short-wavelength bubble, TS denotes the transmitted shock, IRS denotes the shock reflected from the initial interface, SI denotes the shocked interface, TW denotes the transverse waves, CRS denotes the shock reflected from the geometric centre, and TRS denotes the transmitted reflection shock. Curved white arrows represent the orientations that spikes skew towards, and numbers in the images indicate time in $\umu$s.

After the transmitted shock focuses at the geometric centre around 108 $\umu$s, a central reflected shock (CRS) forms and moves outwards (131 $\umu$s). Later, the CRS impacts the evolving dual-mode interface (153 $\umu$s), leading to the phase reversal of the dual-mode interface . The perturbation on the dual-mode interface first decreases to a minimal value (176 $\umu$s) and then increases with an opposite phase to the initial interface perturbation (199 $\umu$s). The reshocked interface consists of a short-wavelength bubble (SB) in the middle with two long-wavelength bubbles (LB) on its two sides. Last, shocks and rarefaction waves are reflected with decreasing strengths between the interface and the geometric centre.

The competition and coalescence of large coherent structures drive the bubble-merging on the reshocked dual-mode interface, resulting in the spikes skewing toward the long-wavelength bubbles (see the white arrows in the 245 $\umu$s image).

The magnitude of the density-gradient field in the simulation is calculated as ,

$$|\nabla\rho| = \left[(\frac{\partial\rho}{\partial x})^2 + (\frac{\partial\rho}{\partial y})^2\right]^{\frac{1}{2}}.$$

The numerical results are shown in the bottom half of the images in figure 4. It can be observed that both waves and interfacial morphologies in simulations qualitatively agree well with the experimental results.

Quantitative analysis

Experimental and numerical results

Due to the nonlinearity of the RM instability , the two initially constituent modes, i.e., modes n_1 and n_2, generate two harmonics with wavenumbers $2n_1$ and $2n_2$, respectively. Moreover, the mode-coupling between the two initially constituent modes generates two couplings with wavenumbers $n_2 + n_1$ and $n_2 - n_1$.

The captured interface morphology is distinct such that the interfacial contour in the experiment can be extracted by an image processing program , as indicated by the insets in figure 5. Spectrum analysis is then performed on the coordinate of the interfacial contour before the interface is reshocked. Notably, since $n_2 = 2n_1$ and $n_1 = n_2 - n_1$ in the experiment, the amplitudes of the harmonic $2n_1$ and coupling $n_2 - n_1$ are superposed on the amplitudes of the mode n_2 and mode n_1, respectively. The time-varying amplitudes of modes n_1 and n_2 and the new harmonic $2n_2$ and coupling $n_2 + n_1$ are then acquired, as shown with square symbols for the experiment and circle symbols for the simulation in figure 5. The amplitude of the mode, harmonic, and coupling with the azimuthal wavenumber n, i.e., a_n, is normalised as $\alpha_n = a_n/a_{n_1}^0$. It can be found that the numerical results quantitatively agrees well with the experimental results, further validating the code utilised in the present study.

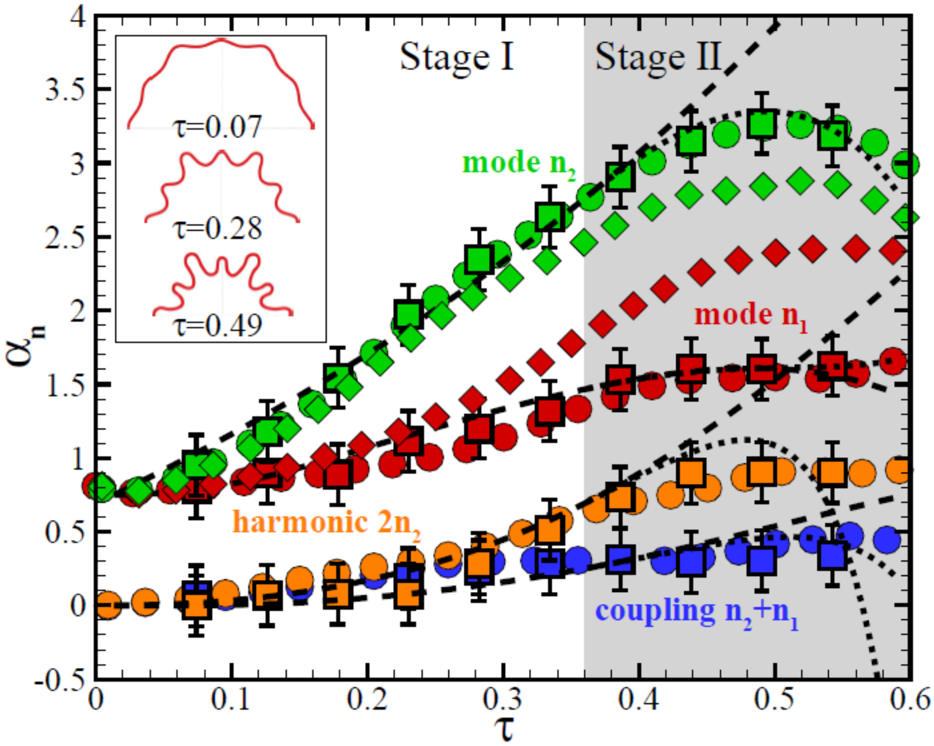

Figure 4 The time-varying dimensionless amplitudes of the two constituent modes (modes n_1 and n_2), and the generated harmonic $2n_1$ and coupling $n_2 + n_1$ obtained from the dual-mode RM instability experiment (square symbols) and simulation (circle symbols). The single-mode RM instabilities of the two constituent modes are numerically calculated and shown with diamond symbols. The dashed lines represent the theoretical predictions in Stage . The dotted lines represent the theoretical predictions in Stage . The inset shows the interfacial contours in the experiment for spectrum analysis.

The amplitude of the mode n_2 is larger than the amplitude of the mode n_1 for two reasons. First, according to the linear solution for the cylindrically convergent RM instability on a single-mode interface with a fixed initial amplitude (see equation ([cylindricalRMI])), the linear amplitude growth rate is larger as n increases. Second, the mode-coupling between modes n_1 and n_2 has a non-negligible influence on the RM instability of the two constituent modes. The amplitude growths of the single-mode RM instability of modes n_1 and n_2 with the same w_0 (= 3.12 mm) are numerically calculated, as shown with diamond symbols in figure 5 for comparisons. It is found that the mode-coupling promotes the RM instability of the higher frequency mode (i.e., mode n_2), but suppresses the RM instability of the lower frequency mode (i.e., mode n_1) in the experiment.

This study intends to quantify the mode-coupling effect on the hydrodynamic instabilities of the dual-mode interface driven by a cylindrically convergent shock and evaluate the time-varying amplitude growths of all first-order modes and second-order harmonics and couplings. The linear solution for the single-mode RM instability (see equation ([cylindricalRMI])) indicates that the RM instability of each mode is related to the variance of the interface radius. Here, the time-varying interface radius R_i and interface velocity v_i are extracted from the 1-D simulation of an unperturbed interface driven by a cylindrically convergent shock using the same initial conditions as the experiment, as shown in figures 7(a) and (b), respectively. It is found that the interface movement can be divided into three stages: Stage . The interface moves inward uniformly with a speed of Δv during $\tau < 0.36$. Stage . The interface moves inward with a decreasing velocity during $0.68 > \tau > 0.36$. If we assume that the interface decelerates at a constant acceleration, then the average acceleration ($\bar{g}$) is about -1.16×10^6 m$\cdot$ s^{-2}. Stage . The interface is reshocked and moves outward when $\tau > 0.68$. In this study, we focus on the hydrodynamic instabilities of the dual-mode interface in Stages and .

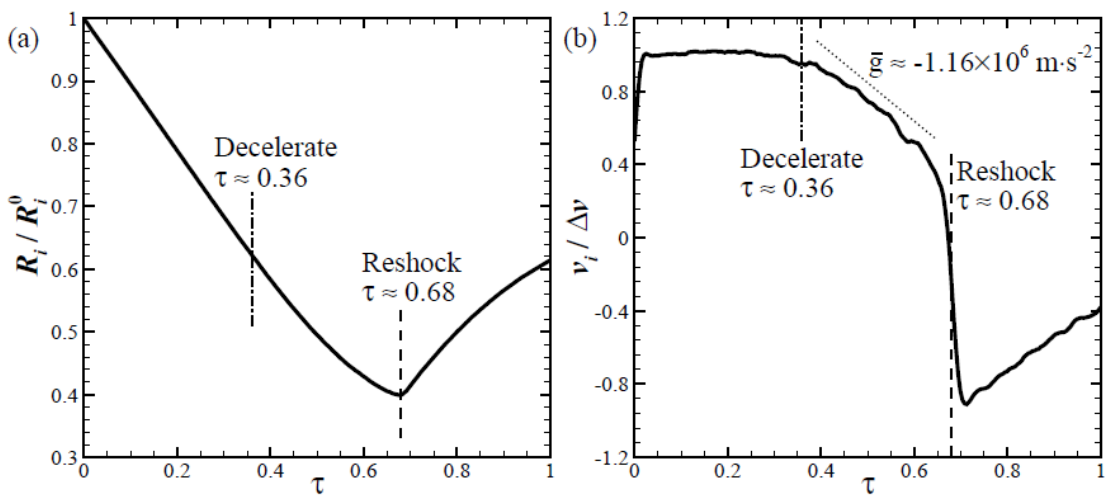

Figure 5. The time-varying dimensionless (a) radius and (b) velocity of an unperturbed interface driven by a cylindrically convergent shock.

Linear and weakly nonlinear solutions

In Stage , the interface motion can be regarded as uniform, and, therefore, the interface radius can be written as $R_i = R_i^0 + \Delta v t$.

Each constituent mode develops linearly at the first-order solution of the RM instability. The first-order linear solutions for the amplitude growth rates of the mode n_1 ($\dot{a}_{n_1}^{\mathrm{RM}}$) and mode n_2 ($\dot{a}_{n_2}^{\mathrm{RM}}$) can be separately written as,

$$\dot{a}_{n_1}^{\mathrm{RM}} = \dot{a}_{n_1}^{\mathrm{I}} C_r,\ \dot{a}_{n_2}^{\mathrm{RM}} = \dot{a}_{n_2}^{\mathrm{I}} C_r,$$

where C_r ($\equiv R_i^0/R_i$) represents the convergence ratio, and its maximum value in the experiment is 2.5; and $\dot{a}_{n_1}^{\mathrm{I}}$ and $\dot{a}_{n_2}^{\mathrm{I}}$ represent the initial amplitude growth rates of the mode n_1 and mode n_2 induced by the RM instability, respectively, and which can be calculated as ,

$$\dot{a}^{\mathrm{I}}_{n_1} = \frac{a^{+}_{n_1} \Delta v (1 - n_1 A)}{R^0_i},\ \dot{a}^{\mathrm{I}}_{n_2} = \frac{a^{+}_{n_2} \Delta v (1 - n_2 A)}{R^0_i}.$$

in which $a^{+}_{n_1}$ ($= (1 - \Delta v / v_s) a^0_{n_1}$) and $a^{+}_{n_2}$ ($= (1 - \Delta v / v_s) a^0_{n_2}$) represent the post-shock amplitudes of the mode n_1 and mode n_2, respectively. When the initial perturbation width of the interface w_0 superposed by multiple modes is comparable to the wavelength of the interface or/and the shock intensity is large, the high-amplitude effect or/and the high-Mach-number effect will inhibit the initial amplitude growth rates . Here, the high-amplitude effect and the high-Mach-number effect on the RM instability are considered independently. Moreover, the startup process before the interface amplitude growth rate reaches the asymptotic value is taken into account. According to , the characteristic times for the startup processes of the mode n_1 ($t^*_{n_1}$) and mode n_2 ($t^*_{n_2}$) can be evaluated as,

$$t^*_{n_1} = \frac{R^0_i}{2n_1} \left(\frac{1 + A}{\Delta v + v_f} + \frac{1 - A}{\Delta v - v_t}\right),\ t^*_{n_2} = \frac{R^0_i}{2n_2} \left(\frac{1 + A}{\Delta v + v_f} + \frac{1 - A}{\Delta v - v_t}\right).$$

Here, we assume that the amplitude growth rates increase linearly from zero to asymptotic values during the startup process.

With the consideration of the high-amplitude effect, the high-Mach-number effect and the startup process, the expressions of the modified initial amplitude growth rates of the mode n_1 and mode n_2 can be separately rewritten as,

$$\dot{a}^{\mathrm{I}}_{n_1} = \frac{H F_{n_1} a^{+}_{n_1} \Delta v (1 - n_1 A) f_{n_1}(t)}{R^0_i},\ \dot{a}^{\mathrm{I}}_{n_2} = \frac{H F_{n_2} a^{+}_{n_2} \Delta v (1 - n_2 A) f_{n_2}(t)}{R^0_i},$$

in which H ($= 1/[1 + (n_{\mathrm{gcd}} w_0 / 6R^0_i)^{(4/3)}]$, with n_{gcd} being the greatest common divisor of n_1 and n_2) is the reduction factor proposed by to quantify the high-amplitude effect; F_{n_1} ($= 1/[1 + \dot{a}^{\mathrm{I}}_{n_1} / (\Delta v - v_t)]$) and F_{n_2} ($= 1/[1 + \dot{a}^{\mathrm{I}}_{n_2} / (\Delta v - v_t)]$) are the reduction factors proposed by to quantify the high-Mach-number effect on the mode n_1 and mode n_2, respectively; and $f_{n_1}(t)$ and $f_{n_2}(t)$ quantify the startup processes of the mode n_1 and mode n_2, respectively, where $f_{n_1}(t) = t/t^*_{n_1}$ if $t < t^*_{n_1}$ and $f_{n_1}(t) = 1$ if $t \geq t^*_{n_1}$, and $f_{n_2}(t) = t/t^*_{n_2}$ if $t < t^*_{n_2}$ and $f_{n_2}(t) = 1$ if $t \geq t^*_{n_2}$.

Based on the perturbation expansion method, and separately derived a second-order solution and a third-order solution for quantifying the nonlinearity of the RM instability by considering the uniform convergence of a single-mode interface. For simplicity, we write the second-order solutions for the amplitude growth rates of the harmonic $2n_1$ ($\dot{a}^{\mathrm{RM}}_{2n_1}$) and harmonic $2n_2$ ($\dot{a}^{\mathrm{RM}}_{2n_2}$) induced by the RM instability as,

$$\dot{a}^{\mathrm{RM}}_{2n_1} = \frac{a^{+}_{n_1} \dot{a}^{\mathrm{I}}_{n_1}}{2R_i} (2An_1 - 1)(C_r - 1) + \frac{(\dot{a}^{\mathrm{I}}_{n_1})^2 t}{6R_i} [(2An_1 - 3)C_r^2 - 8An_1 C_r],$$

$$\dot{a}^{\mathrm{RM}}_{2n_2} = \frac{a^{+}_{n_2} \dot{a}^{\mathrm{I}}_{n_2}}{2R_i} (2An_2 - 1)(C_r - 1) + \frac{(\dot{a}^{\mathrm{I}}_{n_2})^2 t}{6R_i} [(2An_2 - 3)C_r^2 - 8An_2 C_r].$$

Furthermore, extended their previous work and quantified the mode-coupling effect on the convergent RM instability of the mode n at the second-order solution as,

$$\begin{aligned}\frac{\mathrm{d}^2(a_n R_i)}{\mathrm{d}t^2} = \quad & (An-3)\frac{\dot{R}_i^2}{R_i^4}\sum_{n'}(a_{n'}R_i)(a_{n''}R_i) - \\ & (An+1)\frac{1}{R_i^2}\sum_{n'}\frac{\mathrm{d}(a_{n'}R_i)}{\mathrm{d}t}\frac{\mathrm{d}(a_{n''}R_i)}{\mathrm{d}t} - \frac{1}{R_i^2}\sum_{n'}(a_{n''}R_i)\frac{\mathrm{d}^2(a_{n'}R_i)}{\mathrm{d}t^2} + \\ & \frac{\dot{R}_i}{R_i^3}\sum_{n'}\left[(a_{n'}R_i)\frac{\mathrm{d}(a_{n''}R_i)}{\mathrm{d}t} + (a_{n''}R_i)\frac{\mathrm{d}(a_{n'}R_i)}{\mathrm{d}t}\right]\end{aligned}$$

where $n'' = n - n'$. Then, based on equation ([secondorder23]), we can deduce the second-order solutions for the sum and difference couplings, i.e., the amplitude growth rates of the coupling $n_2 + n_1$ ($\dot{a}^{\mathrm{RM}}_{n_2+n_1}$) and coupling $n_2 - n_1$ ($\dot{a}^{\mathrm{RM}}_{n_2-n_1}$) induced by the RM instability as,

$$\begin{aligned}\dot{a}^{\mathrm{RM}}_{n_2+n_1} = \quad & \frac{1}{2R_i}(a^+_{n_2}\dot{a}^{\mathrm{I}}_{n_1} + a^+_{n_1}\dot{a}^{\mathrm{I}}_{n_2})[A(n_2+n_1)-1](C_r-1) + \\ & \frac{\dot{a}^{\mathrm{I}}_{n_1}\dot{a}^{\mathrm{I}}_{n_2}t}{3R_i}[A(n_2+n_1)(C_r^2-4C_r)-3C_r^2],\end{aligned}$$

$$\begin{aligned}\dot{a}^{\mathrm{RM}}_{n_2-n_1} = \quad & \frac{1}{2R_i}\left[A(n_2-n_1)(a^+_{n_2}\dot{a}^{\mathrm{I}}_{n_1} - a^+_{n_1}\dot{a}^{\mathrm{I}}_{n_2}) - (a^+_{n_1}\dot{a}^{\mathrm{I}}_{n_2} + a^+_{n_2}\dot{a}^{\mathrm{I}}_{n_1})\right](C_r-1) + \\ & \frac{\dot{a}^{\mathrm{I}}_{n_1}\dot{a}^{\mathrm{I}}_{n_2}t}{3R_i}[A(n_2-n_1)(C_r^2+2C_r)-3C_r^2].\end{aligned}$$

The first sum terms on the right hand of equations ([secondorder1]) ~ ([secondorder2]) and ([secondorder3])~([secondorder4]) are the linear amplitude growth rates of harmonics $2n_1$ and $2n_2$ and couplings n_2+n_1 and n_2-n_1, respectively. The second sum terms on the right hand of equations ([secondorder1])~([secondorder2]) and ([secondorder3])~([secondorder4]) are the weakly nonlinear modifications of harmonics $2n_1$ and $2n_2$ and couplings n_2+n_1 and n_2-n_1, respectively. The first sum terms indicate that the nonlinearity of the convergent RM instability and the mode-coupling between the two initially constituent modes separately generate new harmonics and couplings from the very beginning, especially when the amplitudes of constituent modes are large, which coincides with our previous study on the multi-mode RM instability in the planar geometry .

Notably, the feedback of harmonics and couplings to the modes owning the same wavenumber influences the RM instability of the initially constituent modes. For example, since $n_2 = 2n_1$ in the experiment, the RM instability of the mode n_1 consists of the amplitude of the mode n_1 at the first-order solution and the amplitude of the coupling $n_2 - n_1$ at the second-order solution; and the RM instability of the mode n_2 consists of the amplitude of the mode n_2 at the first-order solution and the amplitude of the harmonics $2n_1$ at the second-order solution. The theoretical predictions for the time-varying amplitudes of modes n_1 and n_2, the harmonic $2n_2$ and the coupling n_2+n_1 are calculated using equations ([1storder2]), ([1storder4])~([secondorder2]) and ([secondorder3])~([secondorder4]), as shown with dashed lines in figure 5. It is found that the theoretical predictions agree well with the experimental and numerical results before the interface decelerates ($\tau <$ 0.36). When the interface begins to decelerate, the additional RT effect is superimposed on the interface, and, therefore, the theoretical predictions deviate from the experimental and numerical results. For example, the theoretical predictions obviously overestimate the amplitudes of modes and harmonics with large wavenumbers (e.g. mode n_2 and harmonics $2n_2$).

In Stage , the interface decelerates with an average acceleration $\bar{g}$ and can be approximately written as $R_i = R_i^0 + \Delta vt - \frac{1}{2}\bar{g}(t-t^d)^2$, with t^d being the time when the interface begins to decelerate. We only consider the mode-coupling between the two initially modes since the amplitudes of modes n_1 and n_2 are much larger than the generated harmonics and couplings. Similarly, due to the nonlinearity of the RT instability , modes n_1 and n_2 also generate two harmonics with wavenumbers $2n_1$ and $2n_2$, respectively. Moreover, the mode-coupling between modes n_1 and n_2 also generates two couplings with wavenumbers n_2+n_1 and n_2-n_1 .

The first-order linear solutions for the amplitude growth rates of the mode n_1 ($\dot{a}_{n_1}^{\mathrm{RT}}$), mode n_2 ($\dot{a}_{n_2}^{\mathrm{RT}}$), harmonic $2n_2$ ($\dot{a}_{2n_2}^{\mathrm{RT}}$) and coupling n_2-n_1 ($\dot{a}_{n_2-n_1}^{\mathrm{RT}}$) induced by the additional RT effect at a constant acceleration can be written as ,

$$\begin{aligned}
\dot{a}_{n_1}^{\mathrm{RT}} &= -\gamma_{n_1} a_{n_1}^{\mathrm{RM}}(t^d)\sinh(\gamma_{n_1} t^{\xi}),\\
\dot{a}_{n_2}^{\mathrm{RT}} &= -\gamma_{n_2} a_{n_2}^{\mathrm{RM}}(t^d)\sinh(\gamma_{n_2} t^{\xi}),\\
\dot{a}_{2n_2}^{\mathrm{RT}} &= -\gamma_{2n_2} a_{2n_2}^{\mathrm{RM}}(t^d)\sinh(\gamma_{2n_2} t^{\xi}),\\
\dot{a}_{n_2-n_1}^{\mathrm{RT}} &= -\gamma_{n_2-n_1} a_{n_2-n_1}^{\mathrm{RM}}(t^d)\sinh(\gamma_{n_2-n_1} t^{\xi}),
\end{aligned}$$

in which $t^{\xi} = t - t^d$; $\gamma_{n_1} = \sqrt{A\bar{g}n_1/R_i}$, $\gamma_{n_2} = \sqrt{A\bar{g}n_2/R_i}$, $\gamma_{2n_2} = \sqrt{2A\bar{g}n_2/R_i}$ and $\gamma_{n_2-n_1} = \sqrt{A\bar{g}(n_2-n_1)/R_i}$ are the linear growth rates of the mode n_1, mode n_2, harmonic $2n_2$ and coupling n_2-n_1 caused by the additional RT effect, respectively; and $a_{n_1}^{\mathrm{RM}}(t^d)$, $a_{n_2}^{\mathrm{RM}}(t^d)$, $a_{2n_2}^{\mathrm{RM}}(t^d)$ and $a_{n_2-n_1}^{\mathrm{RM}}(t^d)$ are the amplitudes of the mode n_1, mode n_2, harmonic $2n_2$ and coupling n_2-n_1 at t^d, respectively, and which can be calculated by the nonlinear solutions in Stage .

Based on the perturbation expansion method, derived an analytical solution for the RT instability under a constant acceleration considering the geometry convergence effect. At the second-order solutions, the amplitude growth rates of the harmonic $2n_1$ ($\dot{a}_{2n_1}^{\mathrm{RT}}$) and harmonic $2n_2$ ($\dot{a}_{2n_2}^{\mathrm{RT}}$) caused by the additional RT effect can be written as,

$$\dot{a}_{2n_1}^{\mathrm{RT}} = \frac{[a_{n_1}^{\mathrm{RM}}(t^d)]^2}{2R_i}[4(An_1+1)\gamma_1\sinh(\gamma_1 t^\xi)\cosh(\gamma_1 t^\xi) - (2An_1+1)\gamma_{2n_1}\sinh(\gamma_{2n_1} t^\xi)],$$

$$\dot{a}_{2n_2}^{\mathrm{RT}} = \frac{[a_{n_2}^{\mathrm{RM}}(t^d)]^2}{2R_i}[4(An_2+1)\gamma_2\sinh(\gamma_2 t^\xi)\cosh(\gamma_2 t^\xi) - (2An_2+1)\gamma_{2n_2}\sinh(\gamma_{2n_2} t^\xi)].$$

Furthermore, the mode-coupling effect on the RT instability was considered by . The second-order solutions for the amplitude growth rates of the coupling n_2+n_1 ($\dot{a}_{n_2+n_1}^{\mathrm{RT}}$) and coupling n_2-n_1 ($\dot{a}_{n_2-n_1}^{\mathrm{RT}}$) caused by the additional RT effect can be written as,

$$\dot{a}_{n_2+n_1}^{\mathrm{RT}} = \frac{[a_{n_1}^{\mathrm{RM}}(t^d)][a_{n_2}^{\mathrm{RM}}(t^d)]}{2R_i}\{\frac{n_2+n_1}{2\sqrt{n_1 n_2}}[\gamma_{n_1}\cosh(\gamma_{n_1} t^\xi)\sinh(\gamma_{n_2} t^\xi) + \gamma_{n_2}\sinh(\gamma_{n_1} t^\xi)\cosh(\gamma_{n_2} t^\xi)] + [1+A(n_2+n_1)][\gamma_{n_1}\sinh(\gamma_{n_1} t^\xi)\cosh(\gamma_{n_2} t^\xi) + \gamma_{n_2}\cosh(\gamma_{n_1} t^\xi)\sinh(\gamma_{n_2} t^\xi) - \gamma_{n_2+n_1}\sinh(\gamma_{n_2+n_1} t^\xi)]\},$$

$$\dot{a}_{n_2-n_1}^{\mathrm{RT}} = \frac{[a_{n_1}^{\mathrm{RM}}(t^d)][a_{n_2}^{\mathrm{RM}}(t^d)]}{4R_i}\{\sqrt{\frac{n_2}{n_1}}[\gamma_{n_1}\cosh(\gamma_{n_1} t^\xi)\sinh(\gamma_{n_2} t^\xi) + \gamma_{n_2}\sinh(\gamma_{n_1} t^\xi)\cosh(\gamma_{n_2} t^\xi)] + [1-2A(n_2-n_1)][\gamma_{n_1}\sinh(\gamma_{n_1} t^\xi)\cosh(\gamma_{n_2} t^\xi) + \gamma_{n_2}\cosh(\gamma_{n_1} t^\xi)\sinh(\gamma_{n_2} t^\xi) - \gamma_{n_2-n_1}\sinh(\gamma_{n_2-n_1} t^\xi)]\}.$$

The theoretical predictions on the amplitude growths of modes, harmonics and couplings with the same wavenumbers in Stage are calculated by the nonlinear solutions of the RM instability (equations ([1storder2]), ([1storder4])~([secondorder2]) and ([secondorder3])~([secondorder4])) plus the nonlinear solutions of the additional RT effect (equations ([RT1storder2])~([RTsecondorder4])), as shown with dotted lines in figure 5. The theoretical predictions show a better agreement with the experimental and numerical results of the hydrodynamic instabilities of modes n_1 and n_2 and the coupling n_2+n_1 than the instabilities of the harmonic $2n_2$. There are two possible reasons for the poor prediction of the harmonic $2n_2$. On the one hand, as the azimuthal wavenumber n increases, the nonlinearity caused by high-order (third-order and greater) harmonics more influences the instability, and, therefore, the predictions with second-accuracy on the additional RT effect gradually lose their accuracy. On the other hand, we simplify the interface movement in Stage with a constant acceleration, which is different from the actual interface motion with a time-varying acceleration. Since the geometry convergence plays a more important role in the additional RT effect as n increases, the predictions assuming a constant acceleration gradually lose their accuracy. Nevertheless, the theoretical predictions capture the most significant features, i.e., the first-order instabilities of the two constituted modes and the second-order feedback from harmonics and couplings.

Moreover, compared with the prediction that only considers the convergent RM instability, it is found that the additional RT effect suppresses the instabilities of the mode n_2, harmonic $2n_2$ and coupling n_2+n_1, but promotes the instabilities of the mode n_1. This conclusion is different from the convergent RM instability on a single-mode air/SF_6 interface that the additional RT effect always suppresses instability , indicating that the mode-coupling complicates the hydrodynamic instabilities of a multi-mode interface, even resulting in different outcomes of the additional RT effect on the multi-mode interface and single-mode interface.

Parameter analysis

In the second-order solutions for the convergent RM instability and additional RT effect, it is evident that when the wavenumber of one constituent mode of a dual-mode interface is twice the wavenumber of the other constituent mode, the generated second-order harmonics and couplings influence the amplitude growth rates of the two constituent modes since the coupling n_2-n_1 applies the feedback to the mode n_1, and the harmonic $2n_1$ imposes the feedback on the mode n_2. In the experiment, we only consider a specific case where the perturbations on the two constituent modes are in-phase, and the ratio of the amplitude-wavelength-ratios of the two constituent modes δ $(=n_2a_2^0/n_1a_1^0)$ equals 2.0. However, the initial perturbations on the surfaces in applications are random. Therefore, the perturbations on the two constituent modes might be anti-phase, and δ should be various. Numerical simulations on a dual-mode air/SF_6 interface owning the same gas physics parameters as the experiment, but different spectrums with the experiment, are performed to investigate the influences of relative phases and δ on the hydrodynamic instabilities of a dual-mode interface in the cylindrical geometry. The initial spectrum parameters in different cases are listed in table 1.

Table 1 The initial spectrum parameters of the two constituent modes of a dual-mode interface in numerical simulations, where n_1 and n_2 denote the azimuthal wavenumbers of the two constituent modes; a_1^0 and a_2^0 denote the initial amplitudes of the mode n_1 and mode n_2, respectively; w_0 denotes the initial perturbation width of the dual-mode interface; and δ $(=n_2a_2^0/n_1a_1^0)$ denotes the ratio of the amplitude-wavelength-ratios of the two constituent modes.

Case	n_1	n_2	a_1^0 (mm)	a_2^0 (mm)	w_0 (mm)	δ
IP$\udelta$0.25	6	12	1.0	0.125	2.00	0.25
IP$\udelta$1.0	6	12	1.0	0.50	2.25	1.0
IP$\udelta$4.0	6	12	1.0	2.0	5.06	4.0
AP$\udelta$-0.25	6	12	1.0	-0.125	2.00	-0.25
AP$\udelta$-1.0	6	12	1.0	-0.50	2.25	-1.0
AP$\udelta$-4.0	6	12	1.0	-2.0	5.06	-4.0

First, the influences of the phase difference between the two constituent modes on the hydrodynamic instabilities are explored by comparing cases IP$\udelta$2.0 and AP$\udelta$-2.0, as shown in figure 8. Compared with the amplitude growths of single-mode interfaces, the mode-coupling slightly promotes the lower frequency mode (i.e., mode n_1) but slightly suppresses the higher frequency mode (i.e., mode n_2) in the AP$\udelta$-2.0 case, which is different from the IP$\udelta$2.0 case, indicating that the phase difference influences the mode-coupling. Moreover, it is found that the amplitude growth of the coupling $n_2 + n_1$ in the anti-phase case is larger than the in-phase case. In addition, the theoretical predictions of the two constituent modes and two generated harmonics in cases IP$\udelta$2.0 and AP$\udelta$-2.0 are shown with solid and dashed lines, which agree well with the numerical results, further validating the nonlinear solutions.

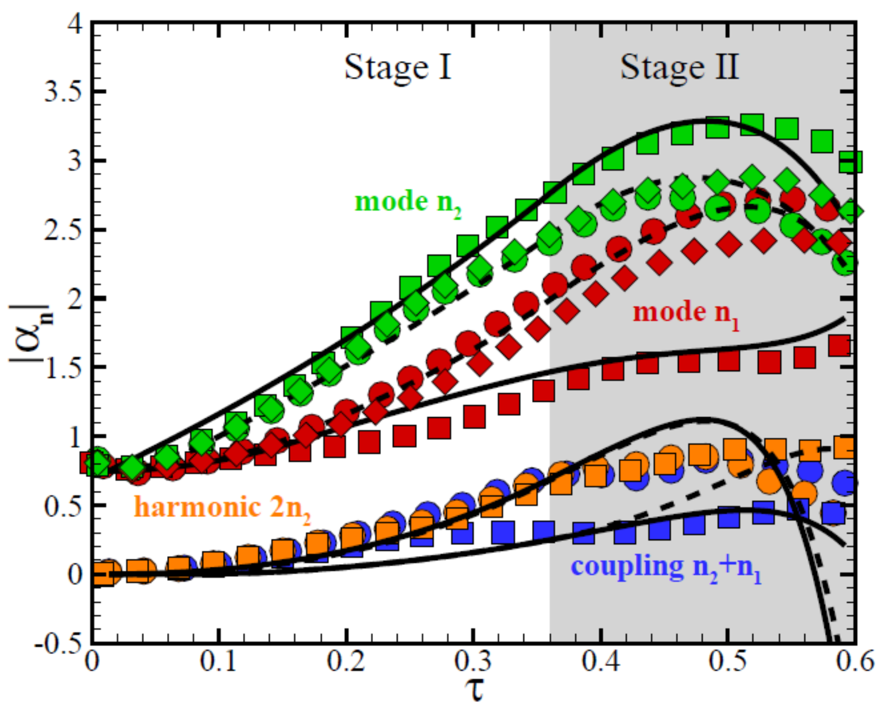

Figure 6 Comparisons of the dimensionless amplitudes of the two constituent modes (modes n_1 and n_2) and the generated harmonic $2n_2$ and coupling $n_2 + n_1$ obtained from the simulations in cases IP$\udelta$2.0 (square symbols) and AP$\udelta$-2.0 (circle symbols), where the single-mode RM instabilities of the two constituent modes are shown with diamond symbols. The solid and dashed lines represent the theoretical predictions for cases IP$\udelta$2.0 and AP$\udelta$-2.0, respectively.

The theoretical predictions for the RM instability and the additional RT effect of all modes, harmonics and couplings in cases IP$\udelta$2.0 and AP$\udelta$-2.0 are shown in figures 10(a) and (b), respectively. In Stage , the influence of phase difference on the RM instability is considered. It is evident that the RM unstable perturbation of the coupling $n_2 - n_1$ grows in the opposite (or same) direction to the RM unstable perturbation of the mode n_1 in the IP$\udelta$2.0 (or AP$\udelta$-

2.0) case. Meanwhile, the RM unstable perturbation of the harmonic $2n_1$ grows in the same (or opposite) direction with the RM unstable perturbation of the mode n_2 in the IP$\udelta$2.0 (or AP$\udelta$-2.0) case. Therefore, the generated coupling $n_2 - n_1$ suppresses the instability of the mode n_1 while the generated harmonic $2n_1$ promotes the instability of the mode n_2 when the two constituent modes are in-phase. Oppositely, the generated coupling $n_2 - n_1$ promotes the instability of the mode n_1 while the generated harmonic $2n_1$ suppresses the instability of the mode n_2 when the two constituent modes are anti-phase.

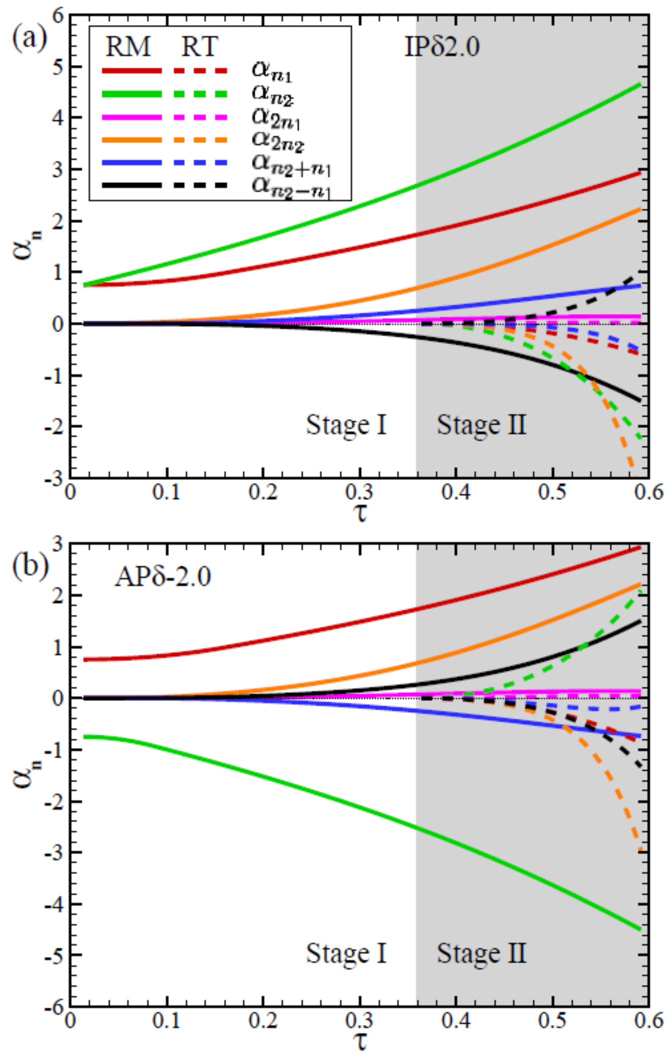

Figure 7. Comparisons of the dimensionless amplitudes of modes, harmonics and couplings predicted by theories in cases (a) IP2.0 and (b) AP-2.0. Solid and dashed lines represent the theoretical predictions for the RM instability and the additional RT effect, respectively.

In Stage , the influence of phase difference on the additional RT effect is considered. It is evident that the RT unstable perturbation of the coupling $n_2 - n_1$ grows in the same (or opposite) direction to the RT unstable perturbation of the mode n_1 in the

IP$\udelta$2.0 (or AP$\udelta$-2.0) case. Meanwhile, the RT unstable perturbation of the harmonic $2n_1$ grows in the same (or opposite) direction with the RT unstable perturbation of the mode n_2 in the IP$\udelta$2.0 (or AP$\udelta$-2.0) case. Therefore, the generated coupling $n_2 - n_1$ and harmonic $2n_1$ separately promote the instabilities of the mode n_1 and mode n_2 when the two constituent modes are in-phase. And the generated coupling $n_2 - n_1$ and harmonic $2n_1$ separately suppress the instabilities of the mode n_1 and mode n_2 when the two constituent modes are anti-phase. However, in the IP$\udelta$2.0 case, the RT unstable perturbation of the coupling $n_2 - n_1$ is larger than that of the mode n_1, therefore the instabilities of the mode n_1 are promoted by the additional RT effect on comparing with the pure RM instability; whereas, the RT unstable perturbation of the harmonic $2n_1$ is smaller than that of the mode n_2, therefore the instabilities of the mode n_2 are suppressed by the additional RT effect on comparing with the pure RM instability.

Moreover, the sign of the perturbation of the coupling $n_2 + n_1$ induced by the additional RT effect is the same as that induced by the RM instability in the IP$\udelta$2.0 case. Differently, the sign of the perturbation of the coupling $n_2 + n_1$ induced by the additional RT effect is opposite to that induced by the RM instability in the AP$\udelta$-2.0 case. Therefore, the amplitude growths of the coupling $n_2 + n_1$ in the anti-phase case are larger than the in-phase case.

Overall, the phase difference influences the mode-coupling mechanism, resulting in different feedbacks of the generated second-order harmonics and couplings to the initially constituent modes, and leading to different outcomes of the RM instability and additional RT effect.

Second, the influences of δ on the instability developments of the two constituent modes are numerically investigated. The initial amplitude of the mode n_1 is fixed as 1.0 mm. The initial amplitudes of the mode n_2 vary from 0.125 mm to 2.0 mm in the five in-phase cases and -0.125 mm to -2.0 mm in the five anti-phase cases. The time-varying dimensionless amplitudes of the two constituent modes in the five in-phase cases and five anti-phase cases are shown in figures 12(a) and (b), respectively.

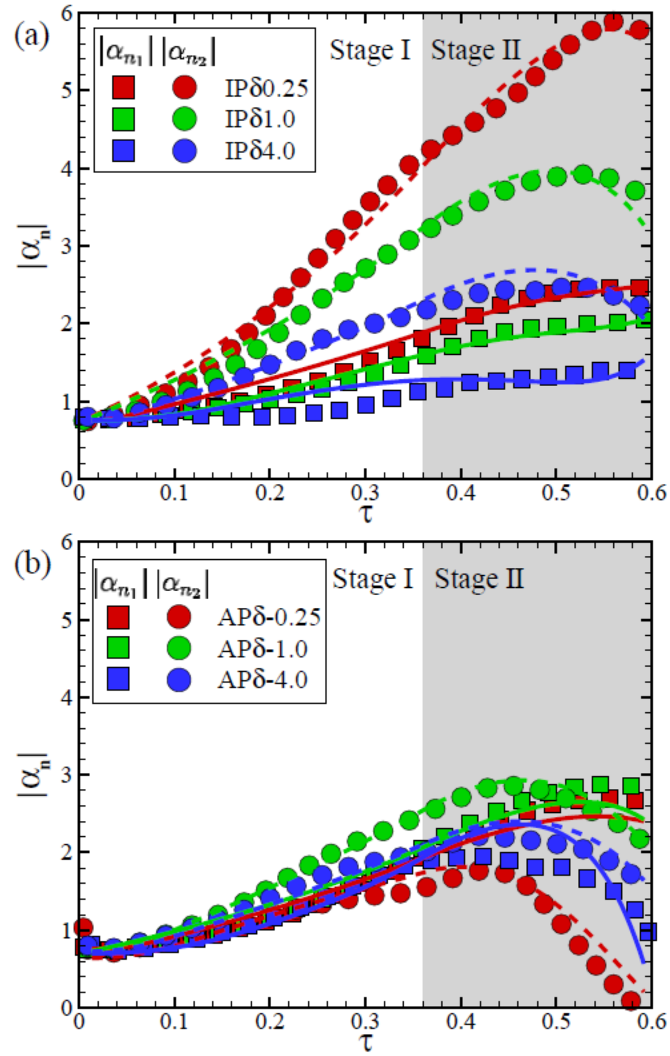

Figure 8. Comparisons of the dimensionless amplitudes of the mode n1 (square symbols) and mode n2 (circle symbols) obtained from numerical simulations in the (a) in-phase cases and (b) anti-phase cases. The solid and dashed lines with colours corresponding to the symbols represent the theoretical predictions for the mode n1 and mode n2, respectively.

In the five in-phase cases, as δ increases, due to the increasing negative feedback of the coupling $n_2 - n_1$ and the increasing suppression introduced by the high-amplitude effect, the amplitude growth of the mode n_1 is more suppressed. As δ increases, due to the decreasing positive feedback of the harmonic $2n_1$ and the increasing suppression introduced by the high-amplitude effect, the amplitude growth of the mode n_1 is more suppressed.

In the five anti-phase cases, as $|\delta|$ increases from 0.25 to 1.0 (or 1.0 to 4.0), the positive feedback of the coupling $n_2 - n_1$ is larger (or less) than the suppression introduced by the high-amplitude effect, and, therefore, the amplitude growth of the mode n_1 is more promoted (or suppressed). Differently, as $|\delta|$ increases from 0.25 to 1.0 (or 1.0 to 4.0), the decreasing negative feedback of the harmonic $2n_1$ is more (or less) significant than the increasing high-amplitude effect, the amplitude growth of the mode n_2 is more promoted (or suppressed).

Overall, the competition between the mode-coupling effect and the high-amplitude effect varies as δ changes, resulting in different outcomes of the RM instability and additional RT effect. It is also noted that the lower frequency mode is largely suppressed when the two constituent modes are in-phase and δ is large, and the higher frequency mode is largely suppressed when the two constituent modes are anti-phase and $|\delta|$ is small. In addition, the theoretical predictions of the hydrodynamic instabilities of the mode n_1 and mode n_2 are shown with solid and dashed lines with colours corresponding to symbols, which agree well with the numerical results, further validating the generality of the nonlinear solutions.

Conclusions

The hydrodynamic instabilities of a dual-mode air/SF_6 interface driven by a cylindrically convergent shock is experimentally examined for the first time. The dual-mode interface is created by an extended soap-film technique in the semi-annular shock tube facility. Precise interfacial morphologies and wave patterns are well captured by high-speed schlieren photography. The influences of the mode-coupling on the RM instability and the additional RT effect of the constituent modes and generated harmonics and couplings from linear to nonlinear stages are theoretically quantified. Numerical simulations solving compressible Euler equations are performed considering various initial spectrums.

The amplitude growths of the initially constituent modes and the second-order harmonics and couplings are obtained by a serial Fourier analysis of the interfacial contours extracted from the schlieren images. A noticeable difference between the growths of the constituent modes and the corresponding single-mode RM instability is observed, suggesting the evident mode-coupling effect on the convergent dual-mode RM instability. A series of analytical, nonlinear solutions with second-order accuracy are adopted by considering the geometry convergence, the mode-coupling mechanism, the high-amplitude effect, the high-Mach-number effect and the startup process to quantify the RM instability and the additional RT effect on the dual-mode interface. The nonlinear solutions well predict the amplitude growths of the first-order modes and the second-order harmonics and couplings before the reshock in the experiment and simulations. The mode-coupling complicates the hydrodynamic instabilities of a multi-mode interface, even resulting in different outcomes of the additional RT effect on the multi-mode interface and single-mode interface.

Referring to the nonlinear solutions, it is evident that when the azimuthal wavenumber of one constituent mode is twice the azimuthal wavenumber of the other constituent mode of a dual-mode interface, the mode-coupling has a non-negligible influence on the hydrodynamic instabilities of the two constituent modes.

Based on the theory and simulations, it is proved that the phase difference and the ratio of the amplitude-wavelength-ratios of the two constituent modes δ greatly influence the mode-coupling mechanism. For a dual-mode interface consisting of in-phase (or anti-phase) modes n and $2n$, the mode-coupling suppresses (or promotes) the instability of the mode n but promotes (or suppresses) the instability of the mode $2n$. Moreover, as δ varies, the competition between the mode-coupling effect and the high-amplitude effect complicates the hydrodynamic instabilities of the constituent modes. For a dual-mode interface, the lower frequency mode is largely suppressed when the two constituent modes are in-phase and δ is large, and the higher frequency mode is largely suppressed when the two constituent modes are anti-phase and $|\delta|$ is small.

Overall, the hydrodynamic instabilities of a multi-mode interface driven by a convergent shock closely depend on the initial spectrums from the very beginning. The mode-coupling mechanism revealed in the convergent dual-mode RM instability and additional RT effect would be of great use for understanding and modelling the hydrodynamic instabilities of a multi-mode interface consisting of random waves. We believe it is an essential step toward the elaborate study of the turbulence driven by a convergent shock.

This work was supported by Tamkeen under the NYU Abu Dhabi Research Institute grant CG002 and Natural Science Foundation of China (Nos. 11772329, 91952205, and 11625211).

REFERENCES

Abarzhi, S. I. 2008 Coherent structures and pattern formation in Rayleigh-Taylor turbulent mixing. Phys. Scr. 78 (1), 015401.

Abarzhi, S. I. 2010 Review of theoretical modelling approaches of Rayleigh-Taylor instabilities and turbulent mixing. Phil. Trans. R. Soc. A 368 (1916), 1809–1828.

Abgrall, R. 1996 How to prevent pressure oscillations in multicomponent flow calculations: a quasi conservative approach. J. Comput. Phys. 125 (1), 150–160.

Alon, U., Hecht, J., Mukamel, D. & Shvarts, D. 1994 Scale invariant mixing rates of hydrodynamically unstable interface. Phys. Rev. Lett. 72, 2867–2870.

Alon, U., Hecht, J., Ofer, D. & Shvarts, D. 1995 Power laws and similarity of Rayleigh-Taylor and Richtmyer-Meshkov mixing fronts. Phys. Rev. Lett. 74, 534–537.

Amendt, P., Colvin, J. D., Ramshaw, J. D., Robey, H. F. & Landen, O. L. 2003 Modified Bell-Plesset effect with compressibility: Application to double-shell ignition target designs. Phys. Plasmas 10 (3), 820–829.

Apazidis, N. & Lesser, M. B. 1996 On generation and convergence of polygonal-shaped shock waves. J. Fluid Mech. 309, 301–319.

Apazidis, N., Lesser, M. B., Tillmark, N. & Johansson, B. 2002 An experimental and theoretical study of converging polygonal shock waves. Shock Waves 12, 39–58.

Balasubramanian, S., Orlicz, G. C. & Prestridge, K. P. 2013 Experimental study of initial condition dependence on turbulent mixing in shock-accelerated Richtmyer-Meshkov fluid layers. J. Turbulence 14 (3), 170–196.

Bell, G. I. 1951 Taylor instability on cylinders and spheres in the small amplitude approxima- tion. Report No. LA-1321, LANL 1321.

Biamino, L., Jourdan, G., Houas, L., Vandenboomgaerde, M. & Souffland, D. 2017 Light/heavy converging Richtmyer-Meshkov instability in a conventional shock tube. In International Symposium on Shock Waves, pp. 595–601. Springer.

Biamino, L., Jourdan, G., Mariani, C., Houas, L., Vandenboomgaerde, M. & Souffland, D. 2015 On the possibility of studying the converging RichtmyerMeshkov instability in a conventional shock tube. Exp. Fluids 56, 26.

Brasseur, M., Vandenboomgaerde, M., Mariani, C., Barros, D. C., Souffland, D. & Jourdan, G. 2021 Experimental generation of spherical converging shock waves. Exp. Fluids 62 (7), 1–8.

Brouillette, M. 2002 The Richtmyer-Meshkov instability. Annu. Rev. Fluid Mech. 34, 445– 468.

Campos, F. C. & Wouchuk, J. G. 2016 Analytical scalings of the linear Richtmyer-Meshkov instability when a shock is reflected. Phys. Rev. E 93 (5), 053111.

Chester, W. 1954 The quasi-cylindrical shock tube. Philos. Mag. 45, 1293–1301.

Chisnell, R. F. 1957 The motion of a shock wave in a channel, with applications to cylindrical and spherical shock waves. J. Fluid Mech. 2, 286–298.

Dell, Z., Stellingwerf, R. F. & Abarzhi, S. I. 2015 Effect of initial perturbation amplitude on Richtmyer-Meshkov flows induced by strong shocks. Phys. Plasmas 22 (9), 092711.

Dell, Z. R., Pandian, A., Bhowmick, A. K., Swisher, N. C., Stanic, M., Stellingw- erf, R. F. & Abarzhi, S. I. 2017 Maximum initial growth-rate of strong-shock-driven Richtmyer-Meshkov instability. Phys. Plasmas 24 (9), 090702.

Di Stefano, C. A., Malamud, G., Kuranz, C. C., Klein, S. R. & Drake, R. P. 2015a Measurement of Richtmyer-Meshkov mode coupling under steady shock conditions and at high energy density. High Energy Density Phys. 17, 263–269.

Di Stefano, C. A., Malamud, G., Kuranz, C. C., Klein, S. R., Stoeckl, C. & Drake,

R. P. 2015b Richtmyer-Meshkov evolution under steady shock conditions in the high- energy-density regime. Appl. Phys. Lett. 106 (11), 114103.

Dimonte, G. & Ramaprabhu, P. 2010 Simulations and model of the nonlinear Richtmyer- Meshkov instability. Phys. Fluids 22, 014104.

Dimonte, G. & Schneider, M. 2000 Density ratio dependence of Rayleigh-Taylor mixing for sustained and impulsive acceleration histories. Phys. Fluids 12, 304–321.

Dimotakis, P. E. & Samtaney, R. 2006 Planar shock cylindrical focusing by a perfect-gas lens. Phys. Fluids 18, 031705.

Ding, J., Deng, X. & Luo, X. 2021 Convergent Richtmyer-Meshkov instability on a light gas layer with perturbed inner and outer surfaces. Phys. Fluids 33 (10), 102112.

Ding, J., Li, J., Sun, R., Zhai, Z. & Luo, X. 2019 Convergent Richtmyer-Meshkov instability of a heavy gas layer with perturbed outer interface. J. Fluid Mech. 878, 277–291.

Ding, J., Liang, Y., Chen, M., Zhai, Z., Si, T. & Luo, X. 2018 Interaction of planar shock wave with three-dimensional heavy cylindrical bubble. Phys. Fluids 30 (10), 106109.

Ding, J., Si, T., Yang, J., Lu, X., Zhai, Z. & Luo, X. 2017a Measurement of a Richtmyer-Meshkov instability at an air-SF6 interface in a semiannular shock tube. Phys. Rev. Lett. 119 (1), 014501.

Ding, J. C., Si, T., Chen, M. J., Zhai, Z. G., Lu, X. Y. & Luo, X. S. 2017b On the interaction of a planar shock with a three-dimensional light gas cylinder. J. Fluid Mech. 828, 289–317.

Drake, R. P. 2018 High-energy-density physics: foundation of inertial fusion and experimental astrophysics. Springer.

Elbaz, Y. & Shvarts, D. 2018 Modal model mean field self-similar solutions to the asymptotic evolution of Rayleigh-Taylor and Richtmyer-Meshkov instabilities and its dependence on the initial conditions. Phys. Plasmas 25 (6), 062126.

Epstein, R. 2004 On the Bell-Plesset effects: the effects of uniform compression and geometrical convergence on the classical Rayleigh-Taylor instability. Phys. plasmas 11 (11), 5114–5124.

Fan, E., Guan, B., Wen, C. Y. & Shen, H. 2019 Numerical study on the jet formation of simple-geometry heavy gas inhomogeneities. Phys. Fluids 31, 026103.

Fincke, J. R., Lanier, N. E., Batha, S. H., Hueckstaedt, R. M., Magelssen, G. R., Rothman, S. D., Parker, K. W. & Horsfield, C. J. 2004 Postponement of saturation of the Richtmyer-Meshkov instability in a convergent geometry. Phys. rev. lett. 93 (11), 115003.

Glendinning, S. G., Colvin, J., Haan, S., Kalantar, D. H., Landen, O. L., Mari- nak, M. M., Remington, B. A., Wallace, R., Cherfils, C., Dague, N., Divol, L.,

Galmiche, D. & Richard, A. L. 2000 Ablation front Rayleigh-Taylor growth experiments in spherically convergent geometry. Phys. Plasmas 7 (5), 2033–2039.

Groom, M. & Thornber, B. 2020 The influence of initial perturbation power spectra on the growth of a turbulent mixing layer induced by Richtmyer-Meshkov instability. Physica D 407, 132463.

Grove, J. W., Holmes, R., Sharp, D. H., Yang, Y. & Zhang, Q. 1993 Quantitative theory of Richtmyer-Meshkov instability. Phys. Rev. Lett. 71, 3473–3476.

Guan, B., Liu, Y., Wen, C.-Y. & Shen, H. 2018 Numerical study on liquid droplet internal flow under shock impact. AIAA J. 56 (9), 3382–3387.

Guo, H. 2018 Theoretical study of weakly nonlinear Rayleigh-Taylor instability in cylindrical implosions. PhD thesis, China Academy of Engineering Physics.

Guo, H., Cheng, T. & Li, Y. 2020 Weakly nonlinear multi-mode Bell-Plesset growth in cylin- drical geometry. Chin. Phys. B 29 (11), 115202.

Guo, H., Wang, L., Ye, W., Wu, J. & Zhang, W. 2018 Weakly nonlinear Rayleigh-Taylor instability in cylindrically convergent geometry. Chin. Phys. Lett. 35 (5), 055201.

Guo, H., Yu, X., Wang, L., Ye, W., Wu, J. & Li, Y. 2014 On the second harmonic generation through Bell-Plesset effects in cylindrical geometry. Chin. Phys. Lett. 31 (4), 044702.

Guo, X., Cong, Z., Si, T. & Luo, X. 2022 Shock-tube studies of single-and quasi-single-mode perturbation growth in Richtmyer-Meshkov flows with reshock. J. Fluid Mech. 941.

Haan, S. W. 1989 Onset of nonlinear saturation for Rayleigh-Taylor growth in the presence of a full spectrum of modes. Phys. Rev. A 39 (11), 5812.

Haan, S. W. 1991 Weakly nonlinear hydrodynamic instabilities in inertial fusion. Phys. Fluids B 3, 2349–2355.

Herrmann, M., Moin, P. & Abarzhi, S. I. 2008 Nonlinear evolution of the Richtmyer-Meshkov instability. J. Fluid Mech. 612, 311–338.

Holmes, R. L., Dimonte, G., Fryxell, B., Gittings, M. L., Grove, J. W., Schneider, M., Sharp, D. H., Velikovich, A. L., Weaver, R. P. & Zhang, Q. 1999 Richtmyer- Meshkov instability growth: Experiment, simulation and theory. J. Fluid Mech. 389, 55–79.

Holmes, R. L. & Grove, J. W. 1995 Numerical investigation of Richtmyer-Meshkov instability using front tracking. J. Fluid Mech. 301, 51–64.

Hosseini, S. H. R. & Takayama, K. 2005 Experimental study of Richtmyer-Meshkov insta- bility induced by cylndrical shock waves. Phys. Fluids 17, 084101.

Igra, D. & Igra, O. 2020 Shock wave interaction with a polygonal bubble containing two different gases, a numerical investigation. J. Fluid Mech. 889.

Jacobs, J. W. & Catton, I. 1988 Three-dimensional Rayleigh-Taylor instability Part 1. Weak- ly nonlinear theory. J. Fluid Mech. 187, 329–352.

Jiang, Y., Wen, C.-Y. & Zhang, D. 2020 Space-time conservation element and solution element method and its applications. AIAA J. 58 (12), 5408–5430.

Kjellander, M., Tillmark, N. & Apazidis, N. 2012 Energy concentration by spherical con- verging shocks generated in a shock tube. Phys. fluids 24 (12), 126103.

Lei, F., Ding, J., Si, T., Zhai, Z. & Luo, X. 2017 Experimental study on a sinusoidal air/SF6 interface accelerated by a cylindrically converging shock. J. Fluid Mech. 826, 819–829.

Leinov, E., Malamud, G., Elbaz, Y., Levin, L. A., Ben-Dor, G. & et al. 2009 Experimental and numerical investigation of the Richtmyer-Meshkov instability under re-shock conditions. J. Fluid Mech. 626, 449–475.

Li, J., Ding, J., Luo, X. & Zou, L. 2022 Instability of a heavy gas layer induced by a cylindrical convergent shock. Phys. Fluids 34 (4), 042123.

Li, J., Ding, J., Si, T. & Luo, X. 2020a Convergent Richtmyer-Meshkov instability of light gas layer with perturbed outer surface. J. Fluid Mech. 884.

Li, M., Ding, J., Zhai, Z., Si, T., Liu, N., Huang, S. & Luo, X. 2020b On divergent Richtmyer-Meshkov instability of a light/heavy interface. J. Fluid Mech. 901.

Li, X., Fu, Y., Yu, C. & Li, L. 2021 Statistical characteristics of turbulent mixing in spherical and cylindrical converging Richtmyer-Meshkov instabilities. J. Fluid Mech. 928.

Liang, Y. 2022a Fundamental Studies of Shock-Driven Hydrodynamic Instabilities. Springer Nature.

Liang, Y. 2022b The phase effect on the Richtmyer-Meshkov instability of a fluid layer. Phys. Fluids 34 (3), 034106.

Liang, Y., Ding, J., Zhai, Z., Si, T. & Luo, X. 2017 Interaction of cylindrically converging diffracted shock with uniform interface. Phys. Fluids 29 (8), 086101.

Liang, Y., Liu, L. & Luo, X. 2022 Experimental study of bubble competition and spike competition in Richtmyer-Meshkov flows. J. Fluid Mech. 949.

Liang, Y., Liu, L., Zhai, Z., Ding, J., Si, T. & Luo, X. 2021 Richtmyer-Meshkov instability on two-dimensional multi-mode interfaces. J. Fluid Mech. 928.

Liang, Y., Zhai, Z., Ding, J. & Luo, X. 2019 Richtmyer-Meshkov instability on a quasi-single-mode interface. J. Fluid Mech. 872, 729–751.

Liang, Y., Zhai, Z. & Luo, X. 2018 Interaction of strong converging shock wave with SF6 gas bubble. Sci. China Phys. Mech. 61 (6), 1–9.

Liang, Y., Zhai, Z., Luo, X. & Wen, C.-Y. 2020 Interfacial instability at a heavy/light interface induced by rarefaction waves. J. Fluid Mech. 885, A42.

Liu, H. & Xiao, Z. 2016 Scale-to-scale energy transfer in mixing flow induced by the Richtmyer- Meshkov instability. Phys. Rev. E 93 (5), 053112.

Liu, L., Liang, Y., Ding, J., Liu, N. & Luo, X. 2018 An elaborate experiment on the single- mode Richtmyer-Meshkov instability. J. Fluid Mech. 853, R2.

Liu, W., He, X. & Yu, C. 2012 Cylindrical effects on Richtmyer-Meshkov instability for arbi- trary Atwood numbers in weakly nonlinear regime. Phys. Plasmas 19 (7), 072108.

Liu, W., Wang, X., Liu, X., Yu, C., Fang, M. & Ye, W. 2020 Pure single-mode Rayleigh-Taylor instability for arbitrary atwood numbers. Sci. Rep. 10 (1), 1–9.

Liu, W., Yu, C., Ye, W., Wang, L. & He, X. 2014 Nonlinear theory of classical cylindrical Richtmyer-Meshkov instability for arbitrary Atwood numbers. Phys. Plasmas 21 (6), 062119.

Liverts, Michael & Apazidis, Nicholas 2016 Limiting temperatures of spherical shock wave implosion. Phys. Rev. Lett. 116, 014501.

Livescu, D. 2020 Turbulence with large thermal and compositional density variations. Annu. Rev. Fluid Mech. 52, 309–341.

Lombardini, M. & Pullin, D.I. 2009a Startup process in the Richtmyer-Meshkov instability. Phys. Fluids 21 (4), 044104.

Lombardini, M. & Pullin, D. I. 2009b Small-amplitude perturbations in the three-dimensional cylindrical Richtmyer-Meshkov instability. Phys. Fluids 21, 114103.

Lombardini, M., Pullin, D. I. & Meiron, D. I. 2014 Turbulent mixing driven by spherical implosions. part 1. flow description and mixing-layer growth. J. Fluid Mech. 748, 85.

Luo, X., Ding, J., Wang, M., Zhai, Z. & Si, T. 2015 A semi-annular shock tube for studying cylindrically converging Richtmyer-Meshkov instability. Phys. Fluids 27 (9), 091702.

Luo, X., Li, M., Ding, J., Zhai, Z. & Si, T. 2019 Nonlinear behaviour of convergent Richtmyer- Meshkov instability. J. Fluid Mech. 877, 130–141.

Luo, X., Liu, L., Liang, Y., Ding, J. & Wen, C.-Y. 2020 Richtmyer-Meshkov instability on a dual-mode interface. J. Fluid Mech. 905, A5.

Luo, X., Si, T., Yang, J. & Zhai, Z. 2014 A cylindrical converging shock tube for shock-interface studies. Rev. Sci. Instrum. 85, 015107.

Luo, X., Zhang, F., Ding, J., Si, T., Yang, J., Zhai, Z. & Wen, C. 2018 Long-term effect of rayleigh-taylor stabilization on converging Richtmyer-Meshkov instability. J. Fluid Mech. 849, 231–244.

Mansoor, M. M., Dalton, S. M., Martinez, A. A., Desjardins, T., Charonko, J. J. & Prestridge, K. P. 2020 The effect of initial conditions on mixing transition of the Richtmyer-Meshkov instability. J. Fluid Mech. 904, A3.

Matsuoka, C. & Nishihara, K. 2006 Fully nonlinear evolution of a cylindrical vortex sheet in incompressible Richtmyer-Meshkov instabilitys. Phys. Rev. E 73, 055304.

Meshkov, E. E. 1969 Instability of the interface of two gases accelerated by a shock wave. Fluid Dyn. 4, 101–104.

Mikaelian, K. O. 1990 Rayleigh-Taylor and Richtmyer-Meshkov instabilities and mixing in stratified spherical shells. Phys. Rev. A 42, 3400.

Mikaelian, K. O. 2005 Rayleigh-Taylor and Richtmyer-Meshkov instabilities and mixing in stratified cylindrical shells. Phys. Fluids 17, 094105.

Miles, A. R. 2004 Bubble merger model for the nonlinear Rayleigh-Taylor instability driven by a strong blast wave. Phys. Plasmas 11, 5140–5155.

Miles, A. R., Edwards, M. J., Blue, B., Hansen, J. F., Robey, H. F., Drake, R. P., Kuranz, C. & Leibrandt, D. R. 2004 The effects of a short-wavelength mode on the evolution of a long-wavelength perturbatoin driven by a strong blast wave. Phys. Plasmas 11, 5507–5519.

Mohaghar, M., Carter, J., Musci, B., Reilly, D., McFarland, J. A. & Ranjan, D. 2017 Evaluation of turbulent mixing transition in a shock-driven variable-density flow. J. Fluid Mech. 831, 779–825.

Niederhaus, C. E. & Jacobs, J. W. 2003 Experimental study of the Richtmyer-Meshkov instability of incompressible fluids. J. Fluid Mech. 485, 243–277.

Niederhaus, J. H. J., Greenough, J. A., Oakley, J. G., Ranjan, D., Anderson, M. H. & Bonazza, R. 2008 A computational parameter study for the three-dimensional shock- bubble interaction. J. Fluid Mech. 594, 85–124.

Nishihara, K., Wouchuk, J. G., Matsuoka, C., Ishizaki, R. & Zhakhovsky, V. V. 2010 Richtmyer-Meshkov instability: theory of linear and nonlinear evolution. Phil. Trans. R. Soc. A 368, 1769–1807.

Ofer, D., Alon, U., Shvarts, D., McCrory, R.L. & Verdon, C.P. 1996 Modal model for the nonlinear multimode Rayleigh-Taylor instability. Phys. Plasmas 3 (8), 3073–3090.

Ofer, D., Shvarts, D., Zinamon, Z. & Orszag, S. A. 1992 Mode coupling in nonlinear Rayleigh-Taylor instability. Phys. Fluids B 4 (11), 3549–3561.

Oron, D., Arazi, L., Kartoon, D., Rikanati, A., Alon, U. & Shvarts, D. 2001 Dimensionality dependence of the Rayleigh-Taylor and Richtmyer-Meshkov instability late-time scaling laws. Phys. Plasmas 8, 2883–2889.

Pandian, A., Stellingwerf, R. F. & Abarzhi, S. I. 2017 Effect of a relative phase of waves constituting the initial perturbation and the wave interference on the dynamics of strong- shock-driven Richtmyer-Meshkov flows. Phys. Rev. Fluids 2 (7), 073903.

Peterson, J. L., Casey, D. T., Hurricane, O. A., Raman, K. S., Robey, H. F. & Sma- lyuk, V. A. 2015 Validating hydrodynamic growth in National Ignition Facility implosions. Phys. Plasmas 22 (5), 056309.

Plesset, M. S. 1954 On the stability of fluid flows with spherical symmetry. J. Appl. Phys. 25, 96–98.

Quirk, J. J. & Karni, S. 1996 On the dynamics of a shock-bubble interaction. J. Fluid Mech. 318, 129–163.

Rayleigh, L. 1883 Investigation of the character of the equilibrium of an incompressible heavy fluid of variable density. Proc. London Math. Soc. 14, 170–177.

Remington, BA, Weber, SV, Marinak, MM, Haan, SW, Kilkenny, JD, Wallace, RJ & Dimonte, G 1995 Single-mode and multimode Rayleigh-Taylor experiments on nova. Phys. Plasmas 2 (1), 241–255.

Richtmyer, R. D. 1960 Taylor instability in shock acceleration of compressible fluids. Commun. Pure Appl. Math. 13, 297–319.

Rikanati, A., Alon, U. & Shvarts, D. 1998 Vortex model for the nonlinear evolution of the multimode Richtmyer-Meshkov instability at low Atwood numbers. Phys. Rev. E 58, 7410–7418.

Rikanati, A., Oron, D., Sadot, O. & Shvarts, D. 2003 High initial amplitude and high Mach number effects on the evolution of the single-mode Richtmyer-Meshkov instability. Phys. Rev. E 67, 026307.

Sadot, O., Erez, L., Alon, U., Oron, D., Levin, L. A., Erez, G., Ben-Dor, G. & Shvarts, D. 1998 Study of nonlinear evolution of single-mode and two-bubble interaction under Richtmyer-Meshkov instability. Phys. Rev. Lett. 80, 1654–1657.

Sembian, S. & Liverts, M. 2020 On using converging shock waves for pressure amplification in shock tubes. Metrologia 57 (3), 035008.

Sembian, S., Liverts, M. & Apazidis, N. 2018 Plane blast wave interaction with an elongated straight and inclined heat-generated inhomogeneity. J. Fluid Mech. 851, 245–267.

Shen, H. & Parsani, M. 2017 The role of multidimensional instabilities in direct initiation of gaseous detonations in free space. J. Fluid Mech. 813.

Shen, H. & Wen, C.-Y. 2016 A characteristic space-time conservation element and solution ele- ment method for conservation laws ii. multidimensional extension. J. Comput Phys 305 (C), 775–792.

Shen, H., Wen, C.-Y., Liu, K. X. & Zhang, D. L. 2015a Robust high-order space-time conservative schemes for solving conservation laws on hybrid meshes. J. Comput Phys 281, 375–402.

Shen, H., Wen, C. Y., Parsani, M. & Shu, C. W. 2017 Maximum-principle-satisfying space- time conservation element and solution element scheme applied to compressible multifluids. J. Comput. Phys. 330, 668–692.

Shen, H., Wen, C.-Y. & Zhang, D. L. 2015b A characteristic space-time conservation element and solution element method for conservation laws. J. Comput Phys 288, 101–118.

Shyue, K. M. 1998 An efficient shock-capturing algorithm for compressible multicomponent problems. J. Comput. Phys. 142 (1), 208–242.

Si, T., Long, T., Zhai, Z. & Luo, X. 2015 Experimental investigation of cylindrical converging shock waves interacting with a polygonal heavy gas cylinder. J. Fluid Mech. 784, 225–251.

Si, T., Zhai, Z. & Luo, X. 2014a Experimental study of Richtmyer-Meshkov instability in a cylindrical converging shock tube. Laser Part. Beams 32, 343–351.

Si, T., Zhai, Z., Luo, X. & Yang, J. 2014b Experimental study on a heavy-gas cylinder accelerated by cylindrical converging shock waves. Shock Waves 24, 3–9.

Smalyuk, V. A., Casey, D. T., Clark, D. S., Edwards, M. J., Haan, S. W., Hamza, A., Hoover, D. E., Hsing, W. W., Hurricane, O., Kilkenny, J. D., Kroll, J., Landen, O. L., Moore, A., Nikroo, A., Peterson, L., Raman, K., Remington, B. A., Robey, H. F., Weber, S. V. & Widmann, K. 2014 First measurements of hydrodynamic instability growth in indirectly driven implosions at ignition-relevant conditions on the national ignition facility. Phys. Rev. Lett. 112 (18), 185003.

Srebro, Y., Elbaz, Y., Sadot, O., Arazi, L. & Shvarts, D. 2003 A general buoyancy-drag model for the evolution of the Rayleigh-Taylor and Richtmyer-Meshkov instabilities. Laser Part. Beams 21, 347–353.

Sun, R., Ding, J., Zhai, Z., Si, T. & Luo, X. 2020 Convergent Richtmyer-Meshkov instability of heavy gas layer with perturbed inner surface. J. Fluid Mech. 902.

Tang, J., Zhang, F., Luo, X. & Zhai, Z. 2021 Effect of atwood number on convergent Richtmyer-Meshkov instability. Acta Mech. Sin. 37 (3), 434–446.

Taylor, G. 1950 The instability of liquid surfaces when accelerated in a direction perpendicular to their planes. I. Proc. R. Soc. Lond. A 201 (1065), 192–196.

Thornber, B. 2016 Impact of domain size and statistical errors in simulations of homogeneous decaying turbulence and the Richtmyer-Meshkov instability. Phys. Fluids 28 (4), 045106. Thornber, B., Drikakis, D., Youngs, D. L. & Williams, R. J. R. 2010 The influence of initial condition on turbulent mixing due to Richtmyer-Meshkov instability. J. Fluid Mech. 654, 99–139.

Thornber, B., Griffond, J., Poujade, O., Attal, N., Varshochi, H., Bigdelou, P., Ramaprabhu, P., Olson, B., Greenough, J., Zhou, Y., Schilling, O., Garside,

K. A., Williams, R. J. R., Batha, C. A., Kuchugov, P. A., Ladonkina, M. E., Tishkin, V. F., Zmitrenko, N. V., Rozanov, V. B. & Youngs, D. L. 2017 Late-time growth rate, mixing, and anisotropy in the multimode narrowband Richtmyer-Meshkov instability: The θ-group collaboration. Phys. Fluids 29 (10), 105107.

Toro, E. F., Spruce, M. & Speares, W. 1994 Restoration of the contact surface in the HLL-Riemann solver. Shock Waves 4 (1), 25–34.

Tubbs, D. L., Barnes, C. W., Beck, J. B., Hoffman, N. M., Oertel, J. A., Watt, R. G., Boehly, T., Bradley, D., Jaanimagi, P. & Knauer, J. 1999 Cylindrical implosion experiments using laser direct drive. Phys. Plasmas 6 (5), 2095–2104.

Vandenboomgaerde, M., Gauthier, S. & Mu¨gler, C. 2002 Nonlinear regime of a multimode Richtmyer-Meshkov instability: A simplified perturbation theory. Phys. Fluids 14 (3), 1111–1122.

Vandenboomgaerde, M., Rouzier, P., Souffland, D., Biamino, L., Jourdan, G., Houas,

L. & Mariani, C. 2018a Nonlinear growth of the converging Richtmyer-Meshkov instabil- ity in a conventional shock tube. Phys. Rev. Fluids 3, 014001.

Vandenboomgaerde, M., Rouzier, P., Souffland, D., Mariani, C., Biamino, L., Jour- dan, G. & Houas, L. 2018b Experimental, numerical and theoretical investigation of the converging Richtmyer-Meshkov instability in a conventional shock tube. In 16th Interna- tional Workshop on the Physics of Compressible Turbulent Mixing .

Velikovich, A. L. & Dimonte, G. 1996 Nonlinear perturbation theory of the incompressible Richtmyer-Meshkov instability. Phys. Rev. Lett. 76 (17), 3112.

Wang, L., Wu, J., Guo, H., Ye, W., Liu, J., Zhang, W. & He, X. 2015 Weakly nonlinear Bell-Plesset effects for a uniformly converging cylinder. Phys. Plasmas 22 (8), 082702.

Wang, L. F., Wu, J. F., Ye, W. H., Zhang, W. Y. & He, X. T. 2013 Weakly nonlinear incompressible Rayleigh-Taylor instability growth at cylindrically convergent interfaces. Phys. Plasmas 20, 042708.

Whitham, G. B. 1958 On the propagation of shock waves through regions of non-uniform area or flow. J. Fluid Mech. 4, 337–360.

Wouchuk, J. G. & Nishihara, K. 1997 Asymptotic growth in the linear Richtmyer-Meshkov instability. Phys. Plasmas 4 (4), 1028–1038.

Wu, J., Liu, H. & Xiao, Z. 2021 Refined modelling of the single-mode cylindrical Richtmyer- Meshkov instability. J. Fluid Mech. 908.

Yan, Z., Fu, Y., Wang, L., Yu, C. & Li, X. 2022 Effect of chemical reaction on mixing transition and turbulent statistics of cylindrical Richtmyer-Meshkov instability. J. Fluid Mech. 941.

Zhai, Z., Li, W., Si, T., Luo, X., Yang, J. & Lu, X. 2017 Refraction of cylindrical converging shock wave at an air/helium gaseous interface. Phys. Fluids 29 (1), 016102.

Zhai, Z., Liang, Y., Liu, L., Ding, J., Luo, X. & Zou, L. 2018a Interaction of rippled shock wave with flat fast-slow interface. Phys. Fluids 30 (4), 046104.

Zhai, Z., Liu, C., Qin, F., Yang, J. & Luo, X. 2010 Generation of cylindrical converging shock waves based on shock dynamcis theory. Phys. Fluids 22, 041701.

Zhai, Z., Ou, J. & Ding, J. 2019a Coupling effect on shocked double-gas cylinder evolution. Phys. Fluids 31 (9), 096104.

Zhai, Z., Si, T., Luo, X., Yang, J., Liu, C. & et al. 2012 Parametric study of cylindri- cal converging shock waves generated based on shock dynamics theory. Phys. Fluids 24, 026101.

Zhai, Z., Zhang, F., Zhou, Z., Ding, J. & Wen, C.-Y. 2019b Numerical study on rayleigh-taylor effect on cylindrically converging richtmyer-meshkov instability. Sci. China Phys. Mech. 62 (12), 1–10.

Zhai, Z., Zou, L., Wu, Q. & Luo, X. 2018b Review of experimental Richtmyer-Meshkov instability in shock tube: From simple to complex. Proc. Inst. Mech. Eng., Part C 232, 2830–2849.

Zhang, Q. & Graham, M. J. 1997 Scaling laws for unstable interfaces driven by strong shocks in cylindrical geometry. Phys. Rev. Lett. 79, 2674–2677.

Zhang, Q. & Graham, M. J. 1998 A numerical study of Richtmyer-Meshkov instability driven by cylindrical shocks. Phys. Fluids 10, 974–992.

Zhang, Q. & Sohn, S. I. 1997 Nonlinear theory of unstable fluid mixing driven by shock wave. Phys. Fluids 9, 1106–1124.

Zhou, Y. 2017a Rayleigh-Taylor and Richtmyer-Meshkov instability induced flow, turbulence, and mixing. I. Phys. Rep. 720-722, 1–136.

Zhou, Y. 2017b Rayleigh-Taylor and Richtmyer-Meshkov instability induced flow, turbulence, and mixing. II. Phys. Rep. 723-725, 1–160.

Zhou, Y., Clark, T. T., Clark, D. S., Glendinning, S. S., Skinner, A. A., Huntington, C., Hurricane, O. A., Dimits, A. M., & Remington, B. A. 2019 Turbulent mixing and transition criteria of flows induced by hydrodynamic instabilities. Phys. Plasmas 26 (8), 080901.

Zhou, Y., Williams, R. J. R., Ramaprabhu, P., Groom, M., Thornber, B., Hillier, A., Mostert, W., Rollin, B., Balachandar, S., Powell, P. D, Mahalovi, A. & Attal, N. 2021

Rayleigh-Taylor and Richtmyer-Meshkov instabilities: A journey through scales. Physica D 423, 132838.

Zhou, Z., Ding, J., Zhai, Z., Cheng, W. & Luo, X. 2020 Mode coupling in converging Richtmyer-Meshkov instability of dual-mode interface. Acta Mech. Sin. 36 (2), 356–366.

Zou, L., Al-Marouf, M., Cheng, W., Samtaney, R., Ding, J. & Luo, X. 2019 Richtmyer-Meshkov instability of an unperturbed interface subjected to a diffracted convergent shock. J. Fluid Mech. 879, 448–467.